# Merging of long rows of plumes: Crosswinds, multiple rows, and applications to cooling towers

Shuo Li ●* and M. R. Flynn ●

*Department of Mechanical Engineering, University of Alberta, Edmonton, Canada AB T6G 1H9*

The merging of a single row of plumes in a quiescent environment has been studied using irrotational flow theory [G. Rooney, J. Fluid Mech. **771**, R1 (2015)]. The present study extends this theory by considering (i) two parallel rows of plumes in a quiescent environment, and (ii) a single row of plumes in a crosswind, with and without a pressure drag term. For plumes in two rows with and without offset, the effect of varying the spacing ratio on the plume dynamics is investigated. Two definitions of the contact height are suggested according to the shape of the velocity potential contours. For a single row of plumes in a crosswind, the governing equations are closed using an entrainment flux evaluated by the irrotational flow theory. This theory predicts the correct near- and far-field similarity solutions in both modest and strong crosswinds. A comparison of the theory in question to previous towing tank experiments yields satisfactory agreement in terms of plume trajectory. The present theory of single and dual rows of plumes is applied to long rows of cooling tower plumes.

## I. INTRODUCTION

Plume merger has been studied under different configurations, including pairs [1,2], rows [3,4], and rosette groups [5] of plumes. In the case of a pair of plumes, a deflection of the plume axes is expected to occur as plumes draw closer together; this a result of restricted entrainment. By contrast, for a long row of plumes, the plumes located far from the ends are not significantly deflected due to the approximately equal but opposite pull exerted by the neighboring plumes. Yannopoulos and Noutsopoulos [3,6] formulated the theories of the so-called entrainment restriction approach (ERA) and of the superposition method (SM), respectively. For two or more buoyant jets, the ERA assumes Gaussian profiles of velocity and concentration as a result of which the differential equations describing momentum and concentration conservation are integrated over a reduced cross-sectional area—see their Fig. 2. Based on the same set of governing equations as in the ERA, the SM developed the superposition solution for any sets of pure jets or pure plumes. Later, Yannopoulos [7] combined the ERA and the SM to propose an advanced and more general integral model of plume merger. Unlike Yannopoulos's models, Rooney [4] proposed a theoretical model whereby the boundaries of a long row of plumes are approximated by the velocity potential contours due to an infinite row of line sinks. Rooney's model predicts the correct near-field (far-field) axisymmetric (two-dimensional) plume similarity solutions. Compared to earlier theoretical models, e.g., those of Yannopoulos [7] and Lai and Lee [5], Rooney's model is simpler and less computationally expensive. Rooney's theory presumes a smooth and gradual transition from an axisymmetric plume
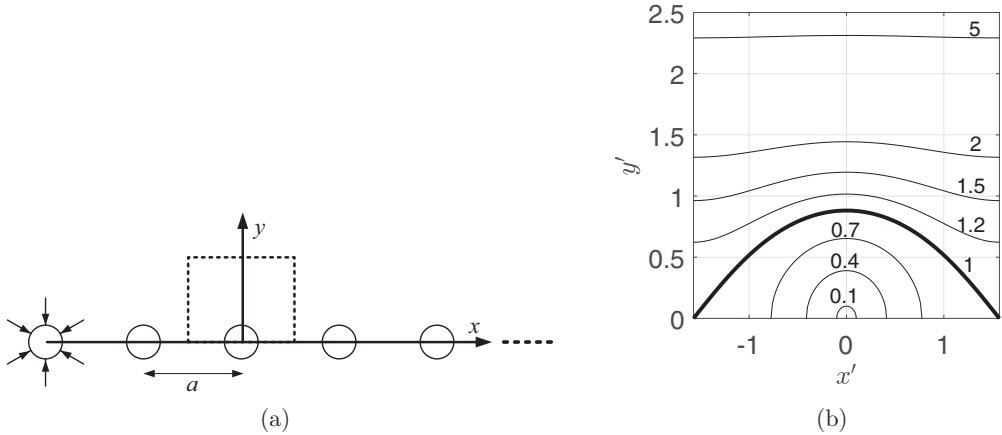
---

*shuo10@ualberta.ca

FIG. 1. (a) Schematic of a single row of equally spaced line sinks. The dashed rectangle indicates the field of view for the contours illustrated in panel (b). (b) Velocity potential contours for a range of $p$, i.e., $p = 0.1$, 0.4, 0.7, 1, 1.2, 1.5, 2, and 5, where $p$ is the constant given in (3). The thick curve, which corresponds to $p = 1$, represents the height of first contact, $\hat{z}_{\mathrm{fc}}$.

to a line plume, which is reflected by the evolution of the velocity potential contours; see, e.g., Fig. 1.

In the case of multiple plumes in a crosswind, the dynamics of any individual plume is influenced by both wind forcing and the entrainment flow field due to the other plumes. Yannopoulos [8] proposed a superposition method to study the merging of a finite row of $n$ plumes in a perpendicular wind. In the $n \to \infty$ limit, Yannopoulos [8] revealed that the ratio of centerline concentrations between $n$ plumes and an isolated plume is $n^{2/3}$, which is consistent with the simple enhancement model of Briggs [9] (cf. Fig. 4 of Ref. [8]). For a rosette group of plumes in a crossflow, Lai and Lee [5] applied a semianalytical model whereby the entrainment field is represented by a distribution of point sinks along the plume centerline trajectory; they found that the interaction between plumes weakens in the presence of a crossflow. Despite the neglect of vortex entrainment in the far field, the model prediction of Lai and Lee [5] is found to be consistent with the experimental results of Lai *et al.* [10]. For multiple tandem plumes in a crossflow, Lai and Lee [11] modeled the blockage and sheltering effect of the leading plume on the rear plume using a distribution of doublets.

Most of the previous studies on plume merger have focused on a single row of plumes; the interactions between two neighboring rows of plumes have not been thoroughly investigated. In the context of cooling towers, a so-called back-to-back configuration, which gives rise to the merging of two rows of plumes, is a popular design alternative because of its ability to dissipate comparatively large amounts of low-grade heat without requiring a large footprint [12]. On the other hand, back-to-back towers may further reduce the rate of entrainment as compared to a single row of towers. This reduced entrainment tends to increase the visible plume length under adverse ambient conditions (i.e. low ambient temperatures and high relative humidities). To this end, insights into the merging of two rows of plumes may benefit cooling tower designs in terms of plume abatement. Of similar importance is to explore a fast and efficient model for describing the merging of a single row of plumes in a crosswind. These twin needs provide the motivation for the present investigation. As such, and following the study of Rooney [4] (R15 hereafter), we shall (i) apply R15 to the case of two parallel rows of plumes arranged with and without offset, and (ii) extend R15 to model a single row of plumes in a windy environment. This latter analysis considers specifically a wind direction that is perpendicular to the row axis so that symmetry is not broken. More generally, goals (i) and (ii) aim to explore the ability of simple irrotational flow theory to describe more complicated plume source conditions and/or ambient conditions.

The paper is organized as follows. Section II reviews the original R15 model. Section III formulates the irrotational flow theory for two rows of plumes with and without offset. Section IV develops the theory for a single row of plumes in a crosswind. Section V applies the present theory to long rows of cooling tower plumes. Conclusions are drawn in Sec. VI.

## II. SINGLE ROW OF INFINITE LINE SINKS [4]

### A. Irrotational flow theory for entrainment flow

R15 considers a single infinite row of equally spaced line sinks spaced at positions $na$ ($n \in \mathbb{Z}$) on the real axis; see Fig. 1(a). Here $a$ is the distance between neighboring plumes. The complex potential due to the whole row of line sinks is

$$\Omega = -\frac{m}{2\pi} \ln \left( \sin \frac{\pi Z}{a} \right) + \Pi, \tag{1}$$

where $Z = x + iy$, $m$ is the strength of a line sink, and $\Pi$ is an arbitrary constant. The velocity potential associated with $\Omega$ is

$$\phi = -\frac{m}{2\pi} \ln \left| \sin \frac{\pi Z}{a} \right| + \Pi = -\frac{m}{2\pi} \ln |\sin x' \cosh y' + i \cos x' \sinh y'| + \Pi, \tag{2}$$

where $x' + iy' = \pi Z/a$. Thus the contours of constant velocity potential are described by

$$\left| \sin \frac{\pi Z}{a} \right| = |\sin (x' + iy')| = p, \tag{3}$$

where $p > 0$ is a constant. Equation (3) can be simplified as

$$\cosh 2y' = \cos 2x' + 2p^2. \tag{4}$$

Expressing $y'$ in terms of $x'$ and $p$ yields

$$y' = \tfrac{1}{2} \ln(2p^2 + \cos 2x' + [(2p^2 + \cos 2x')^2 - 1]^{1/2}). \tag{5}$$

Velocity potential contours are plotted in Fig. 1(b) for a range of $p$. For $0 \leqslant p \leqslant 1$, the roots of $y'$ are $x' = \pm \tfrac{1}{2} \cos^{-1} (1 - 2p^2)$ whereas for $p > 1$, the roots are $x' = \pm \pi/2$. The area under any velocity potential contour, $A' = \pi^2 A/a^2$, is given by

$$A' = \int_{x'_-}^{x'_+} y' dx', \tag{6}$$

where $x'_{\pm} = \pm \tfrac{1}{2} \cos^{-1} (1 - 2p^2)$ for $0 < p \leqslant 1$ and $x'_{\pm} = \pm \pi/2$ for $p > 1$.

The complex velocity is obtained by $\frac{d\Omega}{dZ} = u - iv$, thus

$$\frac{d\Omega}{dZ} = -\frac{m}{2a} \frac{\sin 2x' - i \sinh 2y'}{\cosh 2y' - \cos 2x'}. \tag{7}$$

Hence, the entrainment flow speed, $q = (u^2 + v^2)^{1/2}$, is given by

$$q = \frac{m}{2a} \left( \frac{\cosh 2y' + \cos 2x'}{\cosh 2y' - \cos 2x'} \right)^{1/2} = \frac{m(p^2 + \cos 2x')^{1/2}}{2ap} = \frac{m(\cosh 2y' - p^2)^{1/2}}{2ap}. \tag{8}$$

The speed, $q_e$, of the fluid entrained at $x' = 0$ is given by

$$q_e = \frac{m(p^2 + 1)^{1/2}}{2ap}. \tag{9}$$

Note that $q_e$ is the maximum entrainment speed on a velocity potential contour. The entrainment flux, $E$, across any velocity potential contour is defined as

$$E = \int_{x_-}^{x_+} q \, dl,$$ (10)

and the contour length is given by

$$l' = \frac{\pi}{a} l = \int_{x'_-}^{x'_+} dl'.$$ (11)

It is shown in Appendix A that the entrainment flux across any velocity potential contour equals half the strength of the line sink (this result is not stated explicitly in Ref. [4] due to a possible rounding error; changes resulting from $E = m/2$ have been made in the following sections), i.e., $E = m/2$.

### B. Plume equations and entrainment closure

The generalized plume equations (for a half-plume) are given by

$$A \frac{d}{dz} \left( \frac{1}{2} w^2 \right) = A g' - w E,$$ (12)

$$\frac{d}{dz} (A w) = E,$$ (13)

$$\frac{d}{dz} (A w g') = -A w N^2,$$ (14)

where $w$ is the mean vertical velocity, $g'$ is the reduced gravity, and $N$ is the ambient buoyancy frequency. Equations (13) and (14) can be obtained by reorganizing the original plume equations from the seminal work of Morton *et al.* [13].

Recognizing the need for an entrainment closure, R15 suggested relating $q_e$ with $w$, i.e., $q_e = \alpha w$, where $\alpha$ is an entrainment coefficient. Applying this last result in (9), the strength of the line sink can be expressed as

$$m = 2a \alpha w \frac{p}{(p^2 + 1)^{1/2}}.$$ (15)

Because we have shown that $E = m/2$, the entrainment flux is given by

$$E = m/2 = a \alpha w \frac{p}{(p^2 + 1)^{1/2}},$$ (16)

which serves as the closure condition for (12)–(14).

### C. Merging plumes in an unstratified ambient

For an unstratified ambient with $N = 0$, the buoyancy flux, $F = A w g'$, is constant; see (14). On this basis, (12) and (13) can be rewritten as

$$\frac{dw}{dz} = \frac{F}{Qw} - \frac{a \alpha w^2}{Q} f,$$ (17)

$$\frac{dQ}{dz} = a \alpha w f,$$ (18)

where $Q = A w$ is plume volume flux and

$$f = \frac{p}{(p^2 + 1)^{1/2}} \rightarrow \begin{cases} p, & p \ll 1, \\ 1, & p \gg 1. \end{cases}$$ (19)

In the limit $p \ll 1$, $y'_0 \equiv y'(x' = 0) = \ln[p + (p^2 + 1)^{1/2}] \approx \ln(p + 1) \approx p$. The product $af$ tends to $\pi$ times the plume radius, $ap/\pi$, in the limit $p \ll 1$ and tends to the constant value $a$ in the limit $p \gg 1$.

The dimensionless vertical velocity, $\hat{w}$, volume flux, $\hat{Q}$, and vertical distance, $\hat{z}$, are as follows:

$$w = \alpha^{-1/3} F^{1/3} a^{-1/3} \hat{w}, \quad Q = \alpha^{-1/3} F^{1/3} a^{5/3} \hat{Q}, \quad z = \alpha^{-1} a \hat{z}, \tag{20}$$

where the hatted variables are dimensionless. Therefore, (17) and (18) can be nondimensionalized as

$$\frac{d\hat{w}}{d\hat{z}} = \frac{1}{\hat{Q}\hat{w}} - \frac{\hat{w}^2}{\hat{Q}} f, \tag{21}$$

$$\frac{d\hat{Q}}{d\hat{z}} = \hat{w} f. \tag{22}$$

The dimensionless cross-sectional area is $\hat{A} = \hat{Q}/\hat{w} = A'/\pi^2 = A/a^2$.

In the near-source region of small $p$, the plume is approximately axisymmetric and thus can be characterized by a flux-balance parameter, $\Gamma$, which is defined as [14]

$$\Gamma = \frac{5}{8\pi^{1/2}\alpha} \frac{(2Q)^2(2F)}{(2M)^{5/2}} = \frac{5}{2^{5/2}\pi^{1/2}} \hat{A}^{-1/2} \hat{w}^{-3}, \tag{23}$$

where $M = Qw$ is the momentum flux. To solve (21) and (22), we first choose a small $p$, e.g., 0.05, and then the corresponding cross-sectional area, $\hat{A}$, can be determined from (6). Subsequently, we set the source value of $\Gamma$ [i.e., $\Gamma_0 = \Gamma(z = 0)$], thus the source value of $\hat{w}$ is determined by inverting (23). Equations (21) and (22) are integrated in the range $0.001 \leqslant \hat{z} \leqslant 5$. For $p = 0.05$, the plume source radius, $b_0$, at the initial level $\hat{z} = 0.001$ is $0.05a/\pi$. For a pure plume balance at the source, i.e., $\Gamma_0 = 1$, we adopt the pure plume similarity solution to derive the near source virtual origin, $\hat{z}_{vn}$. In mathematical terms, the correction in question is given by

$$\hat{z}_{vn} \approx \frac{5}{6}\left(\frac{0.05}{\pi}\right) - 0.001. \tag{24}$$

### D. Representative solution

Representative results showing the dimensionless vertical velocity and volume flux with $\Gamma_0 = 1$ are illustrated in Fig. 2. With the near source virtual origin correction (24) applied, the theoretical results closely align with the near-field similarity scaling. The height of first contact, $\hat{z}_{fc} = 0.353$, is defined as the point where $p$ is closest to unity. This height is close to the height of first contact of 0.350 for two axisymmetric plumes [2]. Linearly extrapolating the $\hat{Q}$ data on a Cartesian grid over $4 < \hat{z} \leqslant 5$ yields the far-field line plume virtual origin, $\hat{z}_{vf} = -0.149$, where the volume flux is "zero." To help with visualization, the surface plot illustrating plume merger is shown in Fig. 3.

### III. TWO ROWS OF INFINITE LINE SINKS

#### A. Nonoffset parallel line sinks

##### 1. Complex potential

As shown in Fig. 4(a), we consider two rows of line sinks spaced $2b$ apart in the $y$-direction. Each row consists of an infinite line of sinks at positions $x = na$ ($n \in \mathbb{Z}$). The total complex potential is

$$\Omega = -\frac{m}{2\pi}\left[\ln\left(\sin\frac{\pi(Z - ib)}{a}\right) + \ln\left(\sin\frac{\pi(Z + ib)}{a}\right)\right] + \Pi, \tag{25}$$
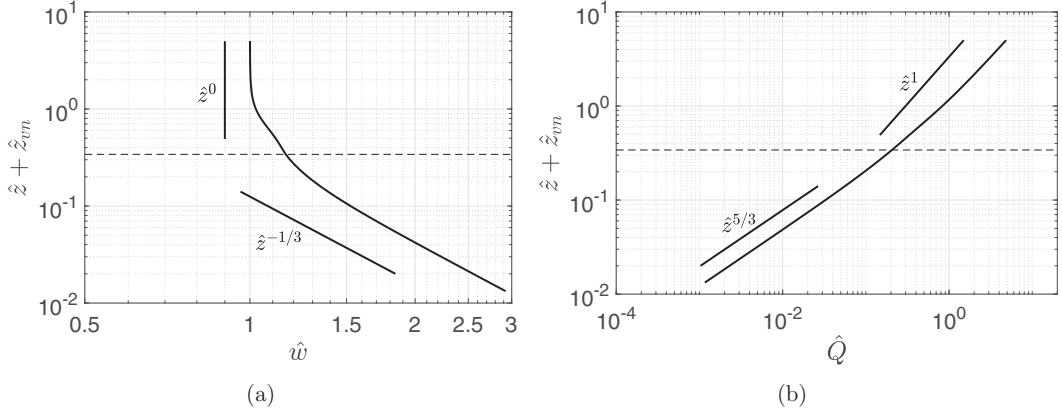
FIG. 2. Evolution of $\hat{w}$ [given by the solution of (21)] and $\hat{Q}$ [given by the solution of (22)] as a function of $\hat{z}$. The horizontal dashed lines denote the height of first contact, $\hat{z}_{fc} = 0.340$. The solid straight lines denote the near-field ($p < 1$) and far-field ($p > 1$) similarity scalings.

where $\Pi$ is an arbitrary constant. The velocity potential is

$$\phi = -\frac{m}{2\pi} \left[ \ln \left| \sin \frac{\pi\,(Z - i\,b)}{a} \right| + \ln \left| \sin \frac{\pi\,(Z + i\,b)}{a} \right| \right] + \Pi \tag{26}$$

$$= -\frac{m}{2\pi} \ln \left| \frac{1}{2} (\cosh 2b' - \cos 2x' \cosh 2y' + i \sin 2x' \sinh 2y') \right| + \Pi, \tag{27}$$

where $x' + iy' = \pi Z/a$ and $b' = \pi b/a$. The contours of constant velocity potential are described by

$$\left| \sin \frac{\pi\,(Z - i\,b)}{a}\, \sin \frac{\pi\,(Z + i\,b)}{a} \right| = p/2, \tag{28}$$

where $p > 0$ is an arbitrary constant. Expanding (28) in terms of $x'$ and $y'$ yields

$$\cosh^2 2y' - 2 \cosh 2b' \cos 2x' \cosh 2y' + \cos^2 2x' + \sinh^2 2b' = p^2. \tag{29}$$
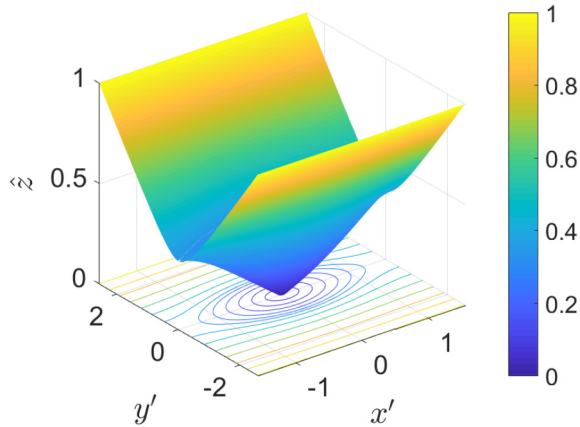


FIG. 3. Surface plot illustrating plume merger in a long row of plumes. The plume boundary is shaded according to the height $0 \leqslant \hat{z} \leqslant 1$.
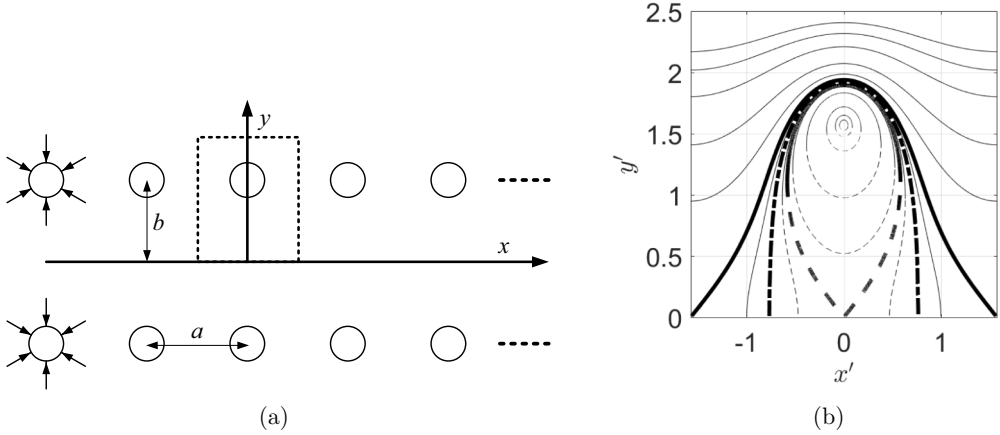
FIG. 4. (a) Schematic of two nonoffset parallel rows of an infinite number of line sinks. The dashed rectangle indicates the field of view for the contours illustrated in panel (b). (b) Velocity potential contours for $b' \equiv \pi b/a = \pi/2$. The contours start from $(0, \pi/2)$ and expand outward with $p$ selected from the set {1, 2, 4, 8, 10, cosh $2b' - 1$, 11, sinh $2b'$, 12, cosh $2b' + 1$, 15, 20, 30, 40, 50}. The thick half-solid and half-dashed contour corresponds to $p = \cosh 2b' - 1$, the thick dash-dotted contour corresponds to $p = \sinh 2b'$, and the thick solid contour that extends into the corners corresponds to $p = \cosh 2b' + 1$. Within the dash-dotted contour ($p < \sinh 2b'$), the solid and dashed parts of the contours correspond, respectively, to the positive and negative roots in (30).

Solving for $y'$ yields

$$\cosh 2y' = \cosh 2b' \cos 2x' \pm (p^2 - \sinh^2 2b' \sin^2 2x')^{1/2}, \tag{30}$$

$$y' = \tfrac{1}{2} \ln[\cosh 2y' + (\cosh^2 2y' - 1)^{1/2}]. \tag{31}$$

We can alternatively solve for $x'$, i.e.,

$$\cos 2x' = \cosh 2b' \cosh 2y' - (p^2 + \sinh^2 2b' \sinh^2 2y')^{1/2}. \tag{32}$$

The negative square root in (30) is applicable for $p < \sinh 2b'$. Equations (30) and (31) indicate that $y'$ is periodic in $x'$ with period $\pi$. The roots of $y'$ are $x' = \pm(1/2) \cos^{-1} (\cosh 2b' - p)$ for cosh $2b' - 1 \leqslant p \leqslant \cosh 2b' + 1$. For $p < \cosh 2b' - 1$, the horizontal range for $x'$ is $-\tfrac{1}{2} \sin^{-1} (p/\sinh 2b') \leqslant x' \leqslant \tfrac{1}{2} \sin^{-1} (p/\sinh 2b')$. Sample velocity potential contours for $b' = \pi/2$ (i.e., $a = 2b$) are illustrated in Fig. 4(b).

The maximum horizontal extent in the $y$-direction, $y'_{\max}$, of each contour occurs at $x' = 0$ where

$$y'_{\max} = \tfrac{1}{2} \ln(\cosh 2b' + p + [2b' + p)^2 - 1]^{1/2})x. \tag{33}$$

The corresponding minimum extent in the $y$-direction is a piecewise function of $p$, and is given by

$$y'_{\min} = \begin{cases} \tfrac{1}{2} \ln(\cosh 2b' - p + [(\cosh 2b' - p)^2 - 1]^{1/2}), & p \leqslant \cosh 2b' - 1, \\ 0, & \cosh 2b' - 1 < p \leqslant \cosh 2b' + 1, \\ \tfrac{1}{2} \ln(-\cosh 2b' + p + [(-\cosh 2b' + p)^2 - 1]^{1/2}), & p > \cosh 2b' + 1. \end{cases} \tag{34}$$

The complex velocity can be obtained from the complex derivative, i.e.,

$$
\begin{aligned}
\frac{d\Omega}{dZ} = u - iv &= -\frac{m}{2a}\left(\cot\frac{\pi\,(Z - i\,b)}{a} + \cot\frac{\pi\,(Z + i\,b)}{a}\right) \\
&= -\frac{m}{a}\,\frac{\cosh 2b'\sin 2x'\cosh 2y' - \frac{1}{2}\sin 4x' + i\big(\cosh 2b'\cos 2x'\sinh 2y' - \frac{1}{2}\sinh 4y'\big)}{\cosh^2 2b' - 2\cosh 2b'\cos 2x'\cosh 2y' + \frac{1}{2}(\cos 4x' + \cosh 4y')}.
\end{aligned}
\tag{35}
$$

The flow speed can be obtained from $q = |\frac{d\Omega}{dZ}|$ and is given by

$$
q^2 = \frac{m^2}{a^2}\,\frac{\big(\cosh 2b'\sin 2x'\cosh 2y' - \frac{1}{2}\sin 4x'\big)^2 + \big(\cosh 2b'\cos 2x'\sinh 2y' - \frac{1}{2}\sinh 4y'\big)^2}{[\cosh^2 2b' - 2\cosh 2b'\cos 2x'\cosh 2y' + \frac{1}{2}(\cos 4x' + \cosh 4y')]^2}.
\tag{36}
$$

Using (29) and (36) is simplified as

$$
q^2 = \frac{m^2}{a^2}\,\frac{\sin^2 2x' + \sinh^2 2y'}{p^2} = \frac{m^2}{a^2}\,\frac{\sin^2 2x' + \cosh^2 2y' - 1}{p^2}.
\tag{37}
$$

At $x' = 0$ and $y' = y'_{\max}$, the characteristic entrainment flow speed is

$$
q_e = \frac{m}{a}\,\frac{\sinh 2y'}{p} = \frac{m}{a}\,\frac{[2b' + p)^2 - 1]^{1/2}}{p}.
\tag{38}
$$

### 2. Flux and area

Differentiating (29) with respect to $x'$ yields

$$
\left(\frac{dy'}{dx'}\right)^2 = \frac{(1 - \cos^2 2x')\,(\cos 2x' - \cosh 2b'\cosh 2y')^2}{(\cosh^2 2y' - 1)\,(\cosh 2y' - \cosh 2b'\cos 2x')^2}.
\tag{39}
$$

Using (30) and (32), respectively, the right-hand side of (39) can be expressed as a function of $x'$ and $p$ or $y'$ and $p$. In turn, the contour length, $l'$, is calculated from

$$
dl' = (dx'^2 + dy'^2)^{1/2} = \left[1 + \left(\frac{dy'}{dx'}\right)^2\right]^{1/2} dx' = \left[1 + \left(\frac{dy'}{dx'}\right)^{-2}\right]^{1/2} dy'.
\tag{40}
$$

For $p \geqslant \cosh 2b' + 1$, $l'$ and the area $A'$ are given by

$$
l' = \int_{x'_-}^{x'_+} \left[1 + \left(\frac{dy'_+}{dx'}\right)^2\right]^{1/2} dx',
\tag{41}
$$

$$
A' = \int_{x'_-}^{x'_+} y'_+ dx',
\tag{42}
$$

where $x'_\pm = \pm\pi/2$, and $y'_+$ corresponds to the positive root in (30). For $\sinh 2b' \leqslant p < \cosh 2b' + 1$, $l'$ and $A'$ are resolved by replacing $x'_\pm = \pm\pi/2$ with $x'_\pm = \pm(1/2)\cos^{-1}(\cosh 2b' - p)$ in both (41) and (42). Conversely when $\cosh 2b' - 1 \leqslant p < \sinh 2b'$, the length and area are evaluated from

$$
l' = 2\int_0^{y'_{\max}} \left[1 + \left(\frac{dy'}{dx'}\right)^{-2}\right]^{1/2} dy',
\tag{43}
$$

$$
A' = 2\int_0^{y'_{\max}} x' dy'.
\tag{44}
$$

Finally for $p < \cosh 2b' - 1$, the length and area are calculated by

$$
l' = \int_{x_{\min}}^{x_{\max}} \left\{\left[1 + \left(\frac{dy'_+}{dx'}\right)^2\right]^{1/2} + \left[1 + \left(\frac{dy'_-}{dx'}\right)^2\right]^{1/2}\right\} dx',
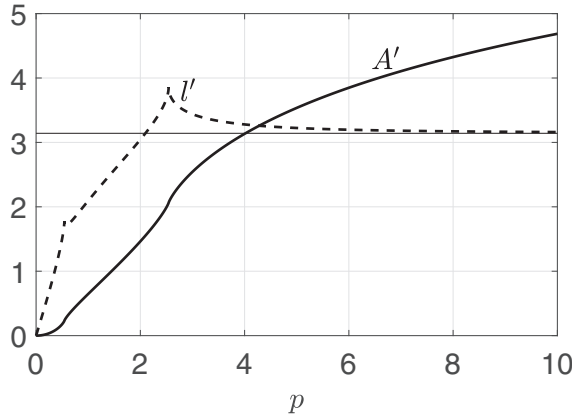\tag{45}
$$

FIG. 5. Contour length, $l'$, and cross-sectional area, $A'$, as a function of $p$ for $b/a = 0.5$. The horizontal line denotes a constant value of $\pi$.

$$A' = \int_{x_{\min}}^{x_{\max}} (y'_+ - y'_-)dx', \tag{46}$$

where $x'_{\min} = -\frac{1}{2} \sin^{-1} (p/\sinh 2b')$, $x'_{\max} = \frac{1}{2} \sin^{-1} (p/\sinh 2b')$, and $y'_-$ corresponds to the negative root in (30). Figure 5 shows $l'$ and $A'$ as a function of $p$.

Analogous to (10), the entrainment flux across an arbitrary velocity potential contour, $C$, is

$$E = \int_C q \, dl = \int_C \frac{a \, q}{\pi} \, dl' = m, \tag{47}$$

where the latter equality applies for all values of $p$; see Appendix A. In turn, the strength of the line sink can be determined by inverting (38), i.e.,

$$m = E = a\alpha w \frac{p}{[(\cosh 2b' + p)^2 - 1]^{1/2}}. \tag{48}$$

Thus the $f$ parameter in (21) and (22) is given by

$$f = \frac{p}{[(\cosh 2b' + p)^2 - 1]^{1/2}}. \tag{49}$$

### 3. Representative solutions

For $b/a = 0.25, 0.5$, and 1 and $\Gamma_0 = 1$, the plume vertical velocity and volume flux are illustrated in Figs. 6(a) and 6(b). Note that here we neglect a near-field virtual origin correction, which does not significantly change the overall profiles. Figure 6(a) shows that the evolution of vertical velocity in the case of a small spacing ratio, i.e., $b/a = 0.25$, is similar to the counterpart evolution for a single row of plumes as shown in Fig. 2(a). By contrast, and for larger values of $b/a$, e.g., $b/a = 1$, there appears a transition zone of almost constant vertical velocity before the far-field limit is approached. Figure 6(b) shows profiles of volume flux for all values of $b/a$.

Two different contact heights are defined: the first contact height, $\hat{z}_{c,1}$, is defined as the elevation where the two opposite plumes first contact one another. This elevation is determined as the point where $p$ is closest to $\cosh 2b' - 1$. The second contact height, $\hat{z}_{c,2}$, is defined as the elevation where the combined plume (postmerger of the two opposite plumes) extends to the corners [see, e.g., the thick solid curve in Fig. 4(b)]. This second contact height is determined as the point where $p$ is closest to $\cosh 2b' + 1$. Interestingly, from $\hat{z}_{c,1}$ to $\hat{z}_{c,2}$ the velocity potential contours move from the stagnation point located at the origin to a stagnation point located in either one of the two corners;
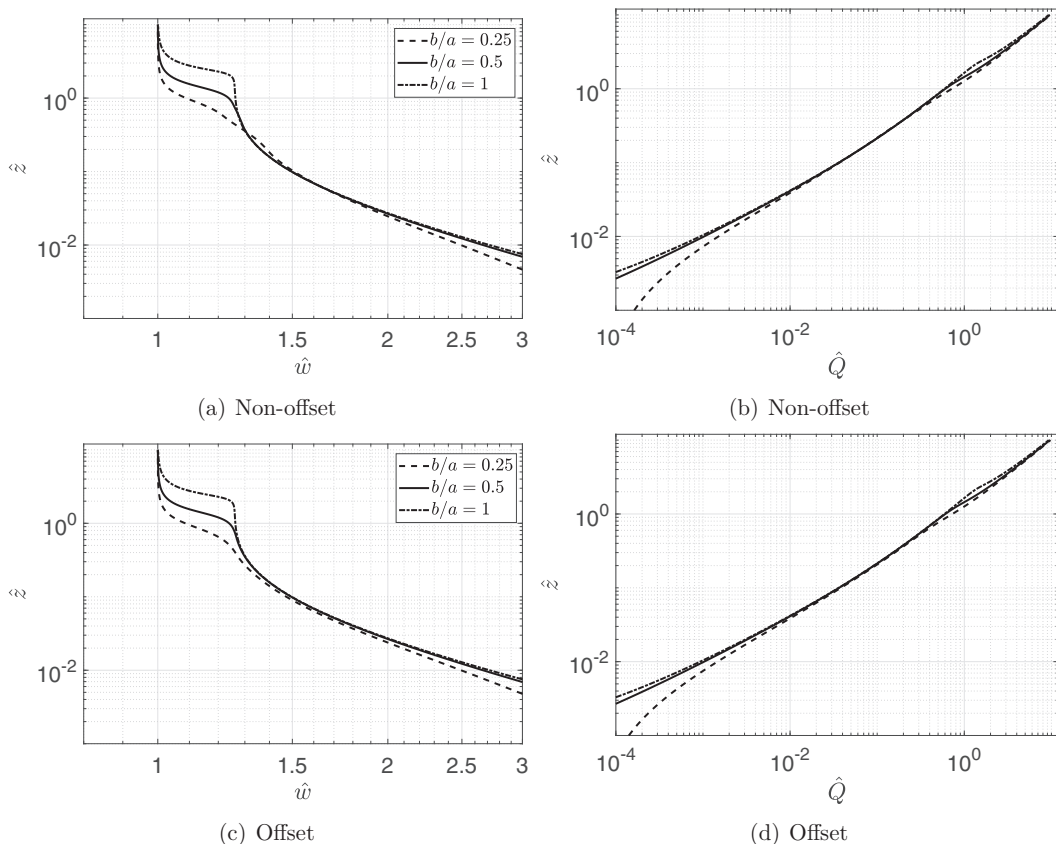
FIG. 6. Evolution of $\hat{w}$ [given by the solution of (21)] and $\hat{Q}$ [given by the solution of (22)] as a function of $\hat{z}$ for spacing ratios of $b/a = 0.25$, 0.5, and 1. Panels (a) and (b) denote the nonoffset case (Fig. 4), whereas panels (c) and (d) denote the offset case (Fig. 9). In all panels, $\Gamma_0 = 1$.

see Fig. 4(b). Note that $\hat{z}_{c,1}$ is similar to the height of first contact for two neighboring axisymmetric plumes (see Fig. 7). Figure 8 indicates that $\hat{z}_{c,1}$ and $\hat{z}_{c,2}$ increase in an approximately linear fashion with $b/a$. In the case of a small $b/a$, e.g., $b/a = 0.05$, $\hat{z}_{c,2} = 0.338$, which is close to the counterpart merger height $\hat{z}_c = 0.340$ for a single row of plumes. In the case of two axisymmetric plumes spaced $2b$ apart, the height of first contact is $z = 0.35(2b/\alpha)$, thus $\hat{z}_c = 0.7b/a$ [2]; this height is somewhat lower than the first contact height for two infinite rows of plumes, i.e., $\hat{z}_{c,1} \approx 0.9b/a$ as inferred from Fig. 8. This difference is likely because, in the latter case, plume distortion is driven by restricted entrainment from two orthogonal directions, i.e., between plumes opposite one another and between neighboring plumes within the same row.

## B. Offset parallel line sinks

### 1. Complex potential

Another typical configuration is two parallel rows of line sinks with an offset ($a/2$) as shown in Fig. 9(a). With this configuration, the complex potential reads

$$\Omega = -\frac{m}{2\pi} \left[ \ln \left( \sin \frac{\pi (Z - i b)}{a} \right) + \ln \left( \cos \frac{\pi (Z + i b)}{a} \right) \right] + \Pi. \tag{50}$$
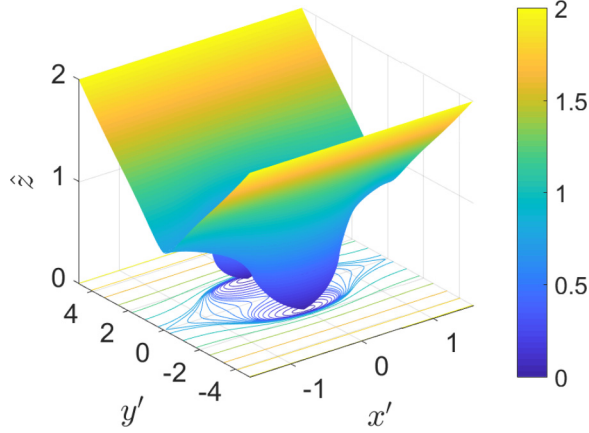
FIG. 7. Surface plot illustrating plume merger in the case of two parallel rows of nonoffset plumes with a spacing ratio of $b/a = 0.5$.

The velocity potential is given by

$$\phi = -\frac{m}{2\pi} \left[ \ln \left| \sin \frac{\pi(Z - ib)}{a} \right| + \ln \left| \cos \frac{\pi(Z + ib)}{a} \right| \right] + \Pi \tag{51}$$

$$= -\frac{m}{2\pi} \ln \left| \frac{1}{2}[\sin 2x' \cosh 2y' + i(\cos 2x' \sinh 2y' - \sinh 2b')] \right| + \Pi. \tag{52}$$

Constant velocity potential contours are given by

$$\left| \sin \frac{\pi(Z - ib)}{a} \cos \frac{\pi(Z + ib)}{a} \right| = p/2, \tag{53}$$

which is simplified as

$$\cosh^2 2y' - 2 \sinh 2b' \cos 2x' \sinh 2y' - \cos^2 2x' + \sinh^2 2b' = p^2. \tag{54}$$
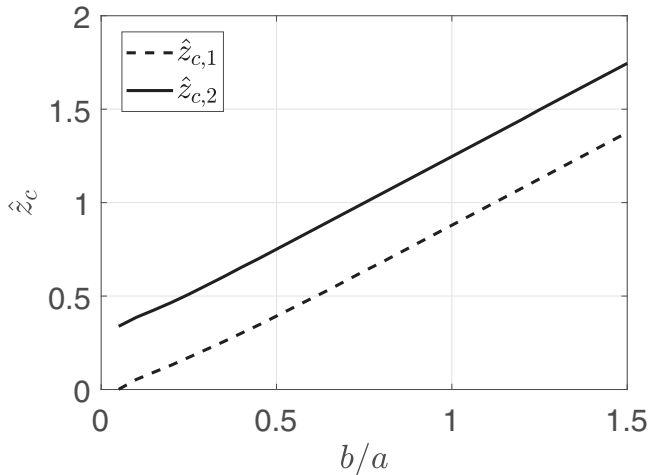


FIG. 8. The contact heights $\hat{z}_{c,1}$ and $\hat{z}_{c,2}$ plotted as a function of the spacing ratio $b/a$. $\hat{z}_{c,1}$ is defined as the elevation where $p$ is closest to $\cosh 2b' - 1$, and $\hat{z}_{c,2}$ is defined as the elevation where $p$ is closest to $\cosh 2b' + 1$. In all cases, $\Gamma_0 = 1$.
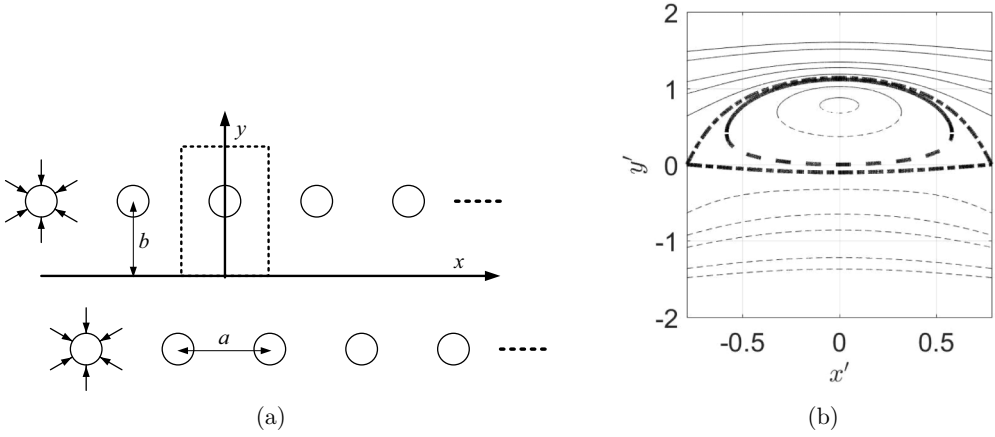
FIG. 9. (a) Schematic of two parallel rows of an infinite number of line sinks with an offset. The dashed rectangle indicates the field of view for the contours illustrated in (b). (b) Velocity potential contours for $b' \equiv \pi b/a = \pi/4$. The contours start from $(0, \pi/4)$ and expand outward with $p$ selected from the set {0.5, 1.5, $\sinh 2b'$, $\cosh 2b'$, 3, 4, 5, 8, 10}. The thick half-solid and half-dashed contour corresponds to $p = \sinh 2b'$, and the dash-dotted contour corresponds to $p = \cosh 2b'$. The solid and dashed curves correspond, respectively, to the positive and negative roots in (55).

Solving for $y'$ yields

$$\sinh 2y' = \sinh 2b' \cos 2x' \pm (p^2 - \cosh^2 2b' \sin^2 2x')^{1/2}, \tag{55}$$

$$y' = \tfrac{1}{2} \ln(\sinh 2y' + (\sinh^2 2y' + 1)^{1/2}), \tag{56}$$

or solving for $x'$ yields

$$\cos 2x' = -\sinh 2b' \sinh 2y' + (\cosh^2 2b' \cosh^2 2y' - p^2)^{1/2}. \tag{57}$$

The positive/negative square roots in (55) are applicable for all values of $p$. Due to the symmetry of the configuration shown in Fig. 9(a), the analysis is restricted to $-\pi/4 \leqslant x' \leqslant \pi/4$. For $\sinh 2b' \leqslant p \leqslant \cosh 2b'$, the roots of $y'$ are $x' = \pm 1/2 \cos^{-1} (\cosh^2 2b' - p^2)^{1/2}$. For $p \leqslant \cosh 2b'$, the horizontal range for $x'$ is $-\tfrac{1}{2} \sin^{-1} (p/\cosh 2b') \leqslant x' \leqslant \tfrac{1}{2} \sin^{-1} (p/\cosh 2b')$. Sample velocity potential contours with $b' = \pi/4$ are illustrated in Fig. 9(b).

The maximum and minimum extents in the $y$-direction are given by

$$y'_{\max} = \tfrac{1}{2} \ln[\sinh 2b' + p + ((\sinh 2b' + p)^2 + 1)^{1/2}], \tag{58}$$

$$y'_{\min} = \tfrac{1}{2} \ln[\sinh 2b' - p + ((\sinh 2b' - p)^2 + 1)^{1/2}], \tag{59}$$

respectively. The complex velocity is obtained from

$$
\begin{aligned}
u &- iv \\
&= -\frac{m}{2a}\left( \cot \frac{\pi(Z - ib)}{a} - \tan \frac{\pi(Z + ib)}{a} \right) \\
&= -\frac{m}{2a} \\
&\quad \times \frac{\sin 4x' \cosh 4y' - 2\sinh 2b' \sin 2x' \sinh 2y' + i(\cos 4x' \sinh 4y' - 2\sinh 2b' \cos 2x' \cosh 2y')}{\cosh^2 2y' - 2\sinh 2b' \cos 2x' \sinh 2y' - \cos^2 2x' + \sinh^2 2b'},
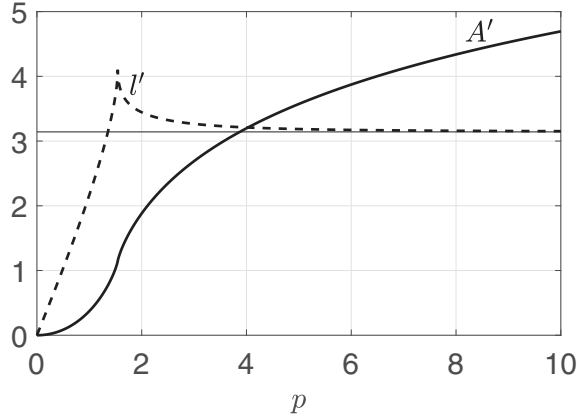\end{aligned}
\tag{60}
$$

FIG. 10. Contour length, $l'$, and cross-sectional area, $A'$, as a function of $p$ for $b/a = 0.5$. The horizontal line denotes a constant value of $\pi$.

thus the flow speed is

$$q^2 = \frac{m^2}{a^2} \frac{\cosh^2 2y' - \sin^2 2x'}{p^2} = \frac{m^2}{a^2} \frac{\sinh^2 2y' + \cos^2 2x'}{p^2}. \tag{61}$$

At $x' = 0$, $y'$ reaches its maximum and the characteristic entrainment speed is given by

$$q_e = \frac{m}{a} \frac{[(\sinh 2b' + p)^2 + 1]^{1/2}}{p}. \tag{62}$$

Differentiation of (54) with respect to $x'$ yields

$$\left(\frac{dy'}{dx'}\right)^2 = \frac{\sin^2 2x'(\sinh 2b' \sinh 2y' + \cos 2x')^2}{\cosh^2 2y'(\sinh 2b' \cos 2x' - \sinh 2y')^2}. \tag{63}$$

The contour length and cross-sectional area can be calculated using a similar approach to that in Sec. III A. Specifically, $l'$ and $A'$ are given by

$$l' = \int_{x'_-}^{x'_+} \left\{ \left[ 1 + \left( \frac{dy'_+}{dx'} \right)^2 \right]^{1/2} + \left[ 1 + \left( \frac{dy'_-}{dx'} \right)^2 \right]^{1/2} \right\} dx', \tag{64}$$

$$A' = \int_{x'_-}^{x'_+} (y'_+ - y'_-) dx', \tag{65}$$

where $x'_\pm = \pm \pi/4$ for $p > \cosh 2b'$, $x'_\pm = \pm \frac{1}{2} \sin^{-1} (p/\cosh 2b')$ for $p \leqslant \cosh 2b'$, and $y'_\pm$ correspond to the positive and negative roots in (55). Figure 10 shows $l'$ and $A'$ as a function of $p$.

Adopting the simple entrainment relation $q_e = \alpha w$, the strength of the line sink, $m$, is thus given by

$$m = a\alpha w \frac{p}{[(\sinh 2b' + p)^2 + 1]^{1/2}}, \tag{66}$$

where, consistent with (47) and (48), $m = E$; see Appendix A. Correspondingly, the parameter $f$ in (21) and (22) is expressed by

$$f = \frac{p}{[(\sinh 2b' + p)^2 + 1]^{1/2}}, \tag{67}$$

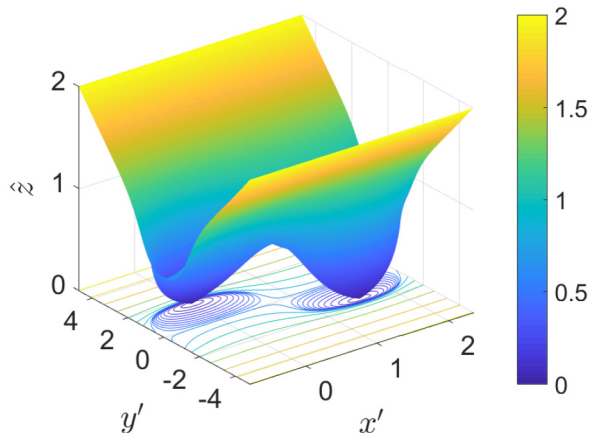which reduces to (19) in the limit $b' \to 0$.

FIG. 11. Surface plot illustrating plume merger in the case of two offset parallel rows of plumes with a spacing ratio of $b/a = 0.5$.

### 2. Representative solutions

For $b/a = 0.25$, 0.5, and 1 and $\Gamma_0 = 1$, Figs. 6(c) and 6(d) show that the vertical velocity and volume flux for the offset case are similar to the counterpart results for the nonoffset case from Figs. 6(a) and 6(b). The vertical velocity profiles are consistent with the shape of velocity potential contours, i.e., the plume boundaries, for different $b/a$ values. Thus for small $b/a$, e.g., $b/a = 0.25$, the contour at the contact height ($p = \cosh 2b'$) is "short and fat"; subsequently this contour evolves like a line plume with a horizontal axis that persists into the very far-field [Fig. 9(b)]. By contrast, the counterpart contour for larger $b/a$, e.g., $b/a = 1$, is expected to be relatively "long and thin," i.e., before approaching its far-field limiting shape, the contour is analogous to a line plume before approaching the far-field limit. The surface plot illustrated in Fig. 11 shows the velocity potential contours at different heights for the case $b/a = 0.5$. We define two different contact heights, $\hat{z}_{c,1}$ and $\hat{z}_{c,2}$, as follows: $\hat{z}_{c,1}$ ($\hat{z}_{c,2}$) is given as the vertical distance where $p$ is closest to $\sinh 2b'$ ($\cosh 2b'$). Physically, $\hat{z}_{c,1}$ is the elevation where an individual plume first touches the center plane [i.e., the $x$ axis in Fig. 9(a)] and $\hat{z}_{c,2}$ is the elevation where plumes on the opposite sides of the $x$ axis contact one another. The contact heights $\hat{z}_{c,1}$ and $\hat{z}_{c,2}$ are illustrated in Fig. 12; differences between $\hat{z}_{c,1}$ and $\hat{z}_{c,2}$ are most apparent for $b/a < 0.5$. Thereafter, and to a very good approximation, $\hat{z}_{c,1} \simeq \hat{z}_{c,2}$. For small $b/a$, the plumes rapidly touch the plane of symmetry (i.e., the $x$-axis) and thereby behave like a single row of plumes. By contrast, and for larger $b/a$, the plume boundary significantly expands in the $x$-direction as the elevation $\hat{z}_{c,1}$ is approached. In turn, such a process of expansion accelerates plume merger so that $\hat{z}_{c,2}$ is only very slightly larger than $\hat{z}_{c,1}$; see, e.g., Fig. 9(b).

### C. Effective entrainment perimeter

Consistent with He and Lou [15], who studied the merger of two adjacent plumes, we have shown in Figs. 5 and 10 that the contour length $l'$ is a nonmonotonic function of $p$, with a "kinky" peak value at the contact height, $\hat{z}_{c,2}$. Due to the discontinuity in $\partial l'/\partial p$, it is expected that the spatial derivative (with respect to $p$) of the entrainment per unit plume perimeter exhibits a singular point at $\hat{z}_{c,2}$. It should be emphasized that the contour length is not directly included in the plume modeling except in the definition of the entrainment flux, i.e., (10). Instead of the plume perimeter, we may consider an "effective entrainment perimeter" to account for the reduced entrainment due to plume merger. The entrainment closure (16) implicitly defines the effective entrainment perimeter, denoted by $P_e$, which is given by
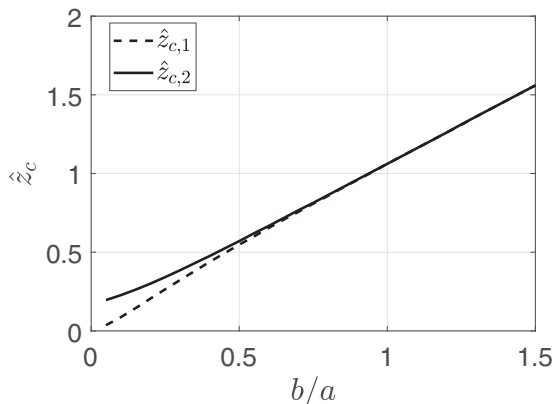
$$P_e = af, \tag{68}$$

FIG. 12. As in Fig. 8 but for the case of offset plumes with an offset distance of $a/2$. $\hat{z}_{c,1}$ is defined as the elevation where $p$ is closest to $\sinh 2b'$, and $\hat{z}_{c,2}$ is defined as the elevation where $p$ is closest to $\cosh 2b'$. In all cases, $\Gamma_0 = 1$.

where $f$ can be specified by either (19), (49), or (67). For single and dual rows of plumes, the evolution of $f = P_e/a$ as a function of $p$ is shown in Fig. 13. The lower value of $f$ for the case of two rows is indicative of the reduced entrainment compared to the single-row case. For a modest spacing ratio of $b/a = 0.2$, Fig. 13 shows that the effective entrainment perimeters for two rows with and without offset are extremely close, which is consistent with the similar profiles shown in Figs. 6(a) and 6(b) and Figs. 6(c) and 6(d). Note that the parameter $f$ is related to the maximum entrainment flow speed on a velocity potential contour. The offset between two rows of plumes does not significantly alter the maximum entrainment flow speed, which occurs at the maximum extent in the $y$ direction.

## IV. PLUME MERGER IN A NEUTRAL CROSSWIND

### A. Formulation

In the case of a crosswind, we assume based on the experimental study of Jordinson [16] that the main mechanism for bending a plume is the rate of entrainment of horizontal momentum from
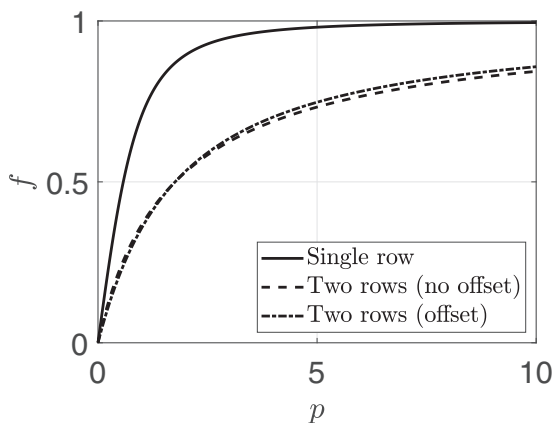


FIG. 13. Nondimensional effective entrainment perimeter as a function of $p$. For two rows of plumes, the spacing ratio is fixed as $b/a = 0.2$.

the ambient to the plume core. Thus each individual plume in a crosswind can still be regarded as a line sink, whose strength is now related to the wind speed. Considering a wind direction that is perpendicular to the axis of a single row of line sinks, the symmetry between individual plumes is not broken. The governing equations are then as follows:

$$\frac{d}{ds}(AU_p) = E,\tag{69}$$

$$\frac{d}{ds}(AU_pu) = EU_a,\tag{70}$$

$$\frac{d}{ds}(AU_pw) = g'A,\tag{71}$$

$$\frac{d}{ds}(AU_pg') = 0,\tag{72}$$

$$\frac{dx}{ds} = \cos\theta,\tag{73}$$

$$\frac{dz}{ds} = \sin\theta,\tag{74}$$

where $U_p$ is the mean streamwise velocity, $u = U_p\cos\theta$ and $w = U_p\sin\theta$ are the horizontal and vertical components of $U_p$, respectively, and $U_a$ is the ambient wind velocity that is assumed to be everywhere uniform. Defining the volume flux, $Q = AU_p$, and buoyancy flux, $F = AU_pg'$, (69)–(71) can be rewritten as

$$\frac{dQ}{ds} = E,\tag{75}$$

$$\frac{du}{ds} = \frac{E(U_a - u)}{Q},\tag{76}$$

$$\frac{dw}{ds} = \frac{F}{Q(u^2 + w^2)^{1/2}} - \frac{wE}{Q}.\tag{77}$$

The above set of equations is closed with an entrainment assumption. Consistent with the irrotational flow theory described in Sec. II, we relate a characteristic entrainment velocity ($q_e$) to the shear between plume and crosswind. One of the simplest forms of entrainment closure has been proposed by Hoult and Weil [17], and it reads

$$q_e = \gamma_1|U_p - U_a\cos\theta| + \gamma_2U_a\sin\theta,\tag{78}$$

where $\gamma_1$ and $\gamma_2$ are entrainment coefficients associated with the longitudinal and transverse shear, respectively. Although $\gamma_1$ tends to vary as the axisymmetric plumes near the source merge into a line plume in the far-field, the theory using a constant entrainment coefficient (see Sec. II) has yielded satisfactory agreement with the experimental data of Bush and Woods [18]. Motivated by this observation, we likewise assume $\gamma_1$ to be constant here.

From (78), the rate of entrainment, $E$, is given by

$$E = 2af(\gamma_1|U_p - U_a\cos\theta| + \gamma_2U_a\sin\theta),\tag{79}$$

where $f$ is to be specified later. Note that the plume in question is a whole plume with $E = m$ rather than the half plume considered in Sec. II. This $E = m$ outcome is consistent with the plume equations (69)–(72) and (75)–(77), which implicitly assume a whole plume. Hereafter, the variables are nondimensionalized using a buoyancy length scale, $L_B = FU_a^{-3}$, and the wind speed, $U_a$, as follows:

$$s = L_B\bar{s}, \quad z = L_B\bar{z}, \quad x = L_B\bar{x}, \quad a = L_B\bar{a},$$

$$u = U_a\bar{u}, \quad w = U_a\bar{w}, \quad U_p = U_a\overline{U}_p = (\bar{u}^2 + \bar{w}^2)^{1/2},$$

$$Q = F^2 U_a^{-5} \overline{Q} = L_B^2 U_a \overline{Q}. \tag{80}$$

On this basis, (75)–(77) are nondimensionalized as

$$\frac{d\overline{Q}}{d\overline{s}} = 2\overline{a} f(\gamma_1 |\overline{U}_p - \cos\theta| + \gamma_2 \sin\theta), \tag{81}$$

$$\frac{d\overline{u}}{d\overline{s}} = 2\overline{a} f \frac{1 - \overline{u}}{\overline{Q}} (\gamma_1 |\overline{U}_p - \cos\theta| + \gamma_2 \sin\theta), \tag{82}$$

$$\frac{d\overline{w}}{d\overline{s}} = \frac{1}{\overline{Q}\,\overline{U}_p} - 2\overline{a} f \frac{\overline{w}}{\overline{Q}} (\gamma_1 |\overline{U}_p - \cos\theta| + \gamma_2 \sin\theta), \tag{83}$$

where $\cos\theta = \frac{\overline{u}}{(\overline{u}^2 + \overline{w}^2)^{1/2}}$, $\sin\theta = \frac{\overline{w}}{(\overline{u}^2 + \overline{w}^2)^{1/2}}$, and $f$ is given by (19). Note that the $f$ of (19) is originally derived for an infinite row of plumes in a quiescent environment. In a weak or moderate crosswind, plume interactions are not expected to be significantly influenced by the crosswind so that (19) remains a reasonable approximation. In a strong crosswind, by contrast, the plumes are rapidly bent over and significant vortex entrainment is anticipated [5]. Such vortex entrainment is not modeled explicitly in the present study. The above simplifying assumption notwithstanding, a comparison between the present theory and the plume merger model of Wu and Koh [19] yields satisfactory agreement; see Appendix B.

The flux-balance parameter is expressed as

$$\Gamma = \frac{5}{8\pi^{1/2}\alpha} \frac{Q^2 F}{M^{5/2}} = \frac{5}{8\pi^{1/2}\alpha} \overline{a}^{-1} A^{*-1/2} \overline{w}^{-3}, \tag{84}$$

where $A^* = A/a^2$ is only a function of $p$. To solve (81)–(83), we first assign a small value of $p$, e.g., $p = 0.05$, thus $A^*$ can be determined from (6) (twice the area because we now consider a whole plume). Then we assign a constant value for $\overline{a}$ and a source value for $\Gamma$ (i.e., $\Gamma_0$), thus the source value of $\overline{w}$, i.e., $\overline{w}_0 \equiv \overline{w}(z = 0)$, can be determined from (84). The source value for $\overline{Q}$ can then be specified from $\overline{Q} = \overline{a}^2 A^* \overline{w}$. The entrainment coefficients are specified as $\alpha = 0.117$, $\gamma_1 = 0.1$, and $\gamma_2 = 0.6$ [20,21].

### B. Near- and far-field similarity scalings

For simplicity, it is assumed that there is no relative motion between the plume and crosswind in the horizontal direction, i.e., $u = U_a$ [22]. Thus, (82) reduces to $\frac{d\overline{u}}{d\overline{s}} = 0$. Moreover, (73) and (74) imply that

$$\overline{w} \equiv \frac{w}{U_a} = \frac{w}{u} = \frac{dz}{dx} = \frac{d\overline{z}}{d\overline{x}}. \tag{85}$$

#### 1. Modest crosswind

In a modest crosswind, the plume trajectory is expected to be quasivertical, which implies that $ds \approx dz$, $U_p \approx w$, and $w \gg U_a$. Moreover, the entrainment in this case is similar to the entrainment in a quiescent environment, thus the entrainment velocity is approximated by

$$q_e = \gamma_1 |U_p - U_a \cos\theta| \approx \gamma_1 U_p \approx \gamma_1 w. \tag{86}$$

With the above simplification, (81) and (83) reduce, respectively, to the following equations:

$$\frac{d\overline{Q}}{d\overline{z}} = 2\gamma_1 \overline{a} f \frac{\overline{M}}{\overline{Q}}, \tag{87}$$

$$\frac{d\overline{M}}{d\overline{z}} = \frac{\overline{Q}}{\overline{M}}, \tag{88}$$

where $\overline{M} = \overline{Q}\,\overline{w} = L_B^{-2}U_a^{-2}M$. In the limit $p \ll 1$, $2af$ tends to $2\pi$ times the plume radius, $ap/\pi$. Thus the cross-sectional area $A = \pi(ap/\pi)^2 = \pi(af/\pi)^2 = Q^2/M$. Then (87) reduces to

$$\frac{d\overline{Q}}{d\overline{z}} = 2\gamma_1(\pi\overline{M})^{1/2}. \tag{89}$$

Solving (88) and (89) yields

$$\overline{Q} = \frac{6\gamma_1}{5}\left(\frac{9\gamma_1}{10}\right)^{1/3}\pi^{2/3}\overline{z}^{5/3}, \quad \overline{M} = \left(\frac{9\gamma_1}{10}\right)^{2/3}\pi^{1/3}\overline{z}^{4/3}, \tag{90}$$

and thus

$$\overline{w} = \frac{5}{6\gamma_1}\left(\frac{9\gamma_1}{10}\right)^{1/3}\pi^{-1/3}\overline{z}^{-1/3}. \tag{91}$$

Equations (89)–(91) are consistent with the classic plume theory of Morton *et al.* [13]. Using (85), $\overline{z}$ is given by

$$\overline{z} = \left(\frac{10}{9\gamma_1}\right)^{1/2}\pi^{-1/4}\overline{x}^{3/4}. \tag{92}$$

In the limit $p \gg 1$, $f \to 1$, thus the solution to (87) and (88) can be obtained as

$$\overline{Q} = (2\gamma_1\overline{a})^{2/3}\overline{z}, \quad \overline{M} = (2\gamma_1\overline{a})^{1/3}\overline{z}, \quad \overline{w} = (2\gamma_1\overline{a})^{-1/3}, \quad \overline{z} = (2\gamma_1\overline{a})^{-1/3}\overline{x}. \tag{93}$$

### 2. Strong crosswind

In the case of a strong crosswind, the plume is a bent-over plume, which implies that $ds \approx dx$, $U_p \approx U_a$, and $w \ll U_a$. The entrainment of a bent-over plume is similar to the entrainment due to a line thermal, which is given by

$$q_e = \gamma_2 U_a \sin\theta \approx \gamma_2 w, \tag{94}$$

thus (81) and (83) can be simplified, respectively, as

$$\frac{d\overline{Q}}{d\overline{x}} = 2\gamma_2\overline{a}f\frac{\overline{M}}{\overline{Q}}, \tag{95}$$

$$\frac{d\overline{M}}{d\overline{x}} = 1. \tag{96}$$

In the limit $p \ll 1$, the cross-sectional area $A = \pi(ap/\pi)^2 = \pi(af/\pi)^2 = Q/U_a$. Thus, (95) reduces to

$$\frac{d\overline{Q}}{d\overline{x}} = 2\gamma_2\pi^{1/2}\overline{Q}^{-1/2}\overline{M}. \tag{97}$$

The solution to (96) and (97) is

$$\overline{Q} = \left(\frac{3\gamma_2}{2}\right)^{2/3}\pi^{1/3}\overline{x}^{4/3}, \quad \overline{M} = \overline{x}, \quad \overline{w} = \left(\frac{2}{3\gamma_2}\right)^{2/3}\pi^{-1/3}\overline{x}^{-1/3}. \tag{98}$$

Using (85), the plume trajectory is given by

$$\overline{z} = \frac{3}{2}\left(\frac{2}{3\gamma_2}\right)^{2/3}\pi^{-1/3}\overline{x}^{2/3}, \tag{99}$$
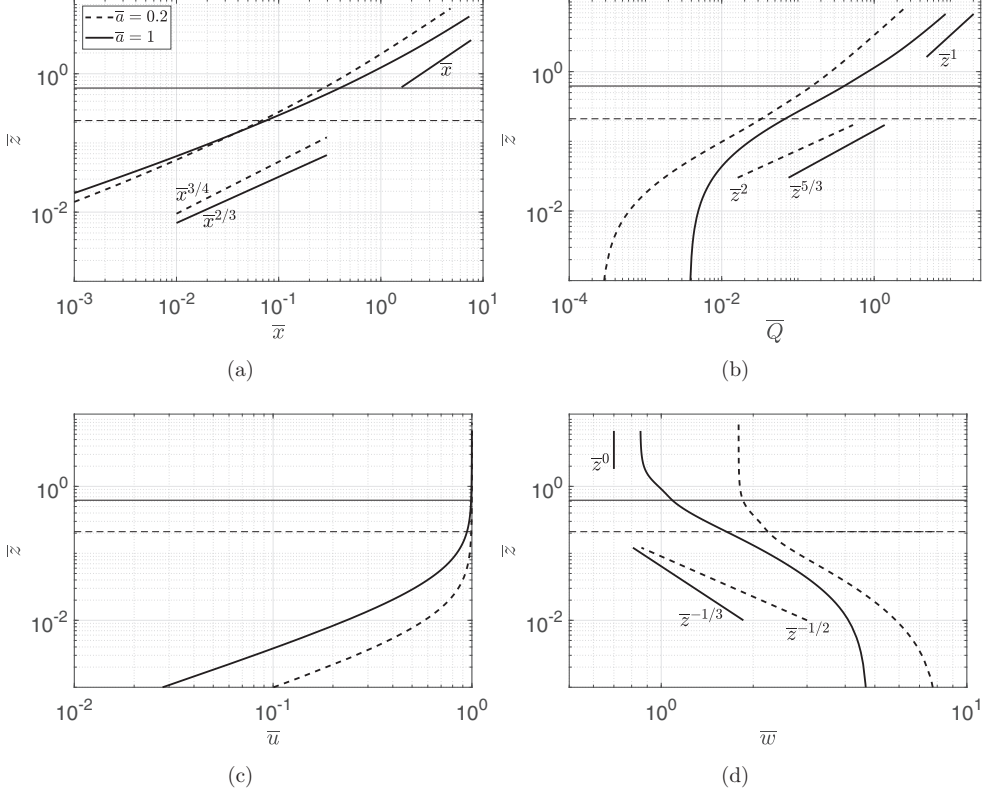
FIG. 14. Evolution of plume trajectory (a), volume flux (b), and horizontal (c) and vertical (d) velocities. The horizontal dashed (solid) line denotes the height of first contact for $\bar{a} \equiv a/L_B = 0.2$ ($\bar{a} = 1$). In both cases, $\Gamma_0 = 1$.

which is consistent with Briggs's classic two-thirds law [23]. Using (99), (98) can be rewritten in terms of $\bar{z}$ as

$$\overline{Q} = \gamma_2^2 \pi \bar{z}^2, \quad \overline{M} = \left(\frac{2}{3}\right)^{1/2} \gamma_2 \pi^{1/2} \bar{z}^{3/2}, \quad \overline{w} = \left(\frac{2}{3}\right)^{1/2} \gamma_2^{-1} \pi^{-1/2} \bar{z}^{-1/2}. \tag{100}$$

In the limit $p \gg 1$, the counterpart solution is given by

$$\overline{Q} = (2\gamma_2 \bar{a})^{1/2} \bar{x}, \quad \overline{M} = \bar{x}, \quad \overline{w} = (2\gamma_2 \bar{a})^{-1/2}, \quad \bar{z} = (2\gamma_2 \bar{a})^{-1/2} \bar{x}. \tag{101}$$

Note from (98) and (101) that $\overline{M}$ has an identical scaling in the near and far fields.

### C. Representative results

For $\bar{a} = 0.2$ and 1 and $\Gamma_0 = 1$, representative results of plume trajectory, volume flux, and horizontal and vertical velocities are illustrated in Fig. 14. The contact heights with $\bar{a} = 0.2$ and 1 are $\bar{z}_c = 0.210$ and 0.621, respectively. Figure 14(a) shows that the plume trajectories for $\bar{a} = 0.2$ and 1 approach the respective near-field scalings $\bar{z} \sim \bar{x}^{3/4}$ and $\bar{z} \sim \bar{x}^{2/3}$, respectively. Nonetheless, the far-field trajectories for both cases follow $\bar{z} \sim \bar{x}$. Analogous near- and far-field similarity scalings for the volume flux and vertical velocity are shown in Figs. 14(b) and 14(d), respectively. Notably, Fig. 14(b) shows that the plume volume flux increases from $\bar{a} = 0.2$ to $\bar{a} = 1$, which is expected because a larger distance between neighboring plumes allows more entrainment. As shown in
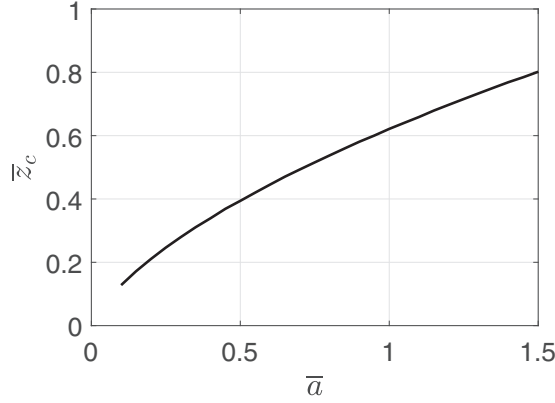
FIG. 15. Contact height, $\bar{z}_c$, as a function of $\bar{a} \equiv a/L_B$. $\bar{z}_c$ is defined as the elevation where $p$ is closest to 1. In all cases, $\Gamma_0 = 1$.

Fig. 14(c), $\bar{u}$ becomes close to unity at small $\bar{z}$, thus the approximation used in (85) is self-consistent. Figure 15 shows that $\bar{z}_c$ increases monotonically with $\bar{a}$.

### D. Additional pressure drag term

Unfortunately, scalings of the type developed in Sec. IV B become more challenging to derive when, as suggested for multiport crossflow discharge by Kannberg and Davis [24], a pressure drag term is supposed to act on each plume. For completeness, in this sub-section we shall elaborate on the significance of such a pressure drag term, recognizing that it is not necessarily required when considering a single plume in a crosswind; see Appendix C. [The comparison between theory and experiment in Appendix C also indicates that assuming a constant, i.e., elevation-independent value for the entrainment coefficients, as we do in Eq. (78), for instance, does not diminish the ability of a theoretical model to yield predictions that are in good agreement with experimental data.] For a row of plumes in a crosswind, the plume-wake interaction or plume downwash is expected to be more pronounced due, e.g., to the blockage of ambient flow postmerger [25]. To account for this effect, integral models, e.g., Ref. [26], have added an extra pressure drag term to allow more plume bending. In a similar fashion, (70) and (71) can be modified, respectively, as

$$\frac{d}{ds}(AU_p u) = EU_a + \frac{1}{2}C_D(U_a \sin\theta)^2 2x_+ \sin\theta, \tag{102}$$

$$\frac{d}{ds}(AU_p w) = g'A - \frac{1}{2}C_D(U_a \sin\theta)^2 2x_+ \cos\theta, \tag{103}$$

where $C_D$ is an empirical drag coefficient and $x_+ = ax'_+$; see (6). Correspondingly, the nondimensional counterpart equations, (82) and (83), are modified, respectively, as follows:

$$\frac{d\bar{u}}{d\bar{s}} = 2\bar{a}f\frac{1-\bar{u}}{\bar{Q}}(\gamma_1|\bar{U}_p - \cos\theta| + \gamma_2 \sin\theta) + C_D\frac{\bar{x}_+}{\bar{Q}}\sin^3\theta, \tag{104}$$

$$\frac{d\bar{w}}{d\bar{s}} = \frac{1}{\bar{Q}\,\bar{U}_p} - 2\bar{a}f\frac{\bar{w}}{\bar{Q}}(\gamma_1|\bar{U}_p - \cos\theta| + \gamma_2 \sin\theta) - C_D\frac{\bar{x}_+}{\bar{Q}}\sin^2\theta \cos\theta, \tag{105}$$

where $x_+ = L_B\bar{x}_+$ and $\bar{x}_+ = x'_+\bar{a}/\pi$. For simplicity, we choose a constant value of $C_D = 1$, which is similar both to the value employed by Wu and Koh [19] and also to the value suggested by the resistance diagram for circular cylinders; see, e.g., Fig. 10.23 of Ref. [27].

### E. Comparison with the towing tank experiments of Ref. [24]

Kannberg and Davis [24] studied the dilution and trajectory of multiport diffusers in a flowing environment. Although a finite row of diffusers was used in their experiments, image walls were added to emulate the effect of an infinite row of plumes in a crosswind. The main control parameters were as follows: source densimetric Froude number, $\mathrm{Fr}_0 = w_0/(g_0' D)^{1/2}$, where $D$ is the port diameter; ratio of the ambient velocity to the plume source velocity, $R = U_a/w_0$; and ratio of the port spacing to the port diameter, $a/D$. Kannberg and Davis [24] considered different angles (denoted by $\theta_0$) between the plume source velocity and the ambient current velocity; however, we shall only consider the perpendicular configuration, i.e., $\theta_0 = \pi/2$, for a comparison between theory and experiment. The measured parameter of particular interest is the plume centerline trajectory, which consists of a set of points $(X/D, Y/D)$, where $X$ and $Y$ are the respective horizontal and vertical distances from the port source. A goal of their experiments was to study the effects of Froude number ($\mathrm{Fr}_0$), velocity ratio ($R$), and port spacing ($a/D$) on the plume trajectory. The main parameters in Ref. [24] can be related to the variables in Sec. IV A as follows:

$$\Gamma_0 = \frac{5}{16\alpha}\mathrm{Fr}_0, \quad \bar{a} = \frac{4}{\pi}\frac{a}{D}\mathrm{Fr}_0^2 R^3, \quad A_0^* \equiv A^*(z=0) = \frac{\pi}{4}\left(\frac{a}{D}\right)^{-2},$$

$$X/D = \frac{a}{D}\frac{\bar{x}}{\bar{a}}, \quad Y/D = \frac{a}{D}\frac{\bar{z}}{\bar{a}}. \tag{106}$$

A comparison of the present theory with (thick curves) and without (thin curves) a pressure drag term to Kannberg and Davis's experiments is presented in Fig. 16, which focuses, in particular, on the plume trajectory. It can be seen that adding a pressure drag term generally improves the agreement between theory and experiment, especially in the relatively far-field. Some moderate mismatch in the near field is due likely to the neglect of the near-source flow development zone in the theory. Notwithstanding this point, there is a nontrivial difference between theory and experiment for the $a/D = 2.5$ case illustrated in Fig. 16(d). This mismatch is consistent with Fig. 5 of Ref. [28], although in this latter case a greater drag coefficient, i.e., $C_D = 3$, is used when $R = 0.10$. In reconciling this difference, it should be emphasized that of all the $a/D = 2.5$ cases in Figs. 16(c)–16(f), the ambient speed $U_a$ for Fig. 16(d) is the smallest, so likewise for the ambient Reynolds number. This Reynolds number is defined as $\mathrm{Re}_a = U_a D/\nu$, where $\nu$ is the kinematic viscosity of the ambient fluid. As argued by Schatzmann and Policastro [26], $\mathrm{Re}_a$ determines the size of the wake zone. We expect, in other words, that the $a/D = 2.5$ data from Fig. 16(d) are significantly impacted by enhanced wake effects. Although we do not pursue this line of inquiry here, it may be necessary to modify the value for $C_D$ in such instances.

## V. APPLICATIONS TO COOLING TOWERS

A major motivation for this study stems from evaluating the visible plume length in cases of back-to-back cooling towers versus a single row of tower cells. Typical ambient conditions and cooling tower operating conditions are listed in Table I. Specifically, each row contains a finite number of $n = 15$ cooling tower cells; see the top-view schematic shown in Fig. 17. Among these cooling tower cells, those of particular concern are the cells at the center and the end points. For a single row, the axis of the plume at the center is not deflected due to symmetry, which is analogous to a plume in an infinite row of plumes. Thus the plume at the center, if not in the very far-field, can be modeled using the analysis in Sec. II. The half plumes at the two ends are, on the other hand, exempt from plume merger and they entrain ambient fluid like an isolated plume. Therefore, the center plume and the plumes at the two sides lead to the least and largest amount of entrainment, respectively; they also represent the "worst" and "best" scenarios in the case of visible plumes. For the counterpart dual rows of plumes, the two center plumes are similar to plumes in the two infinite-row configurations. By contrast, the two half round plumes on each side may be approximated by the merging of two adjacent axisymmetric plumes. Using the same terminology as above, the
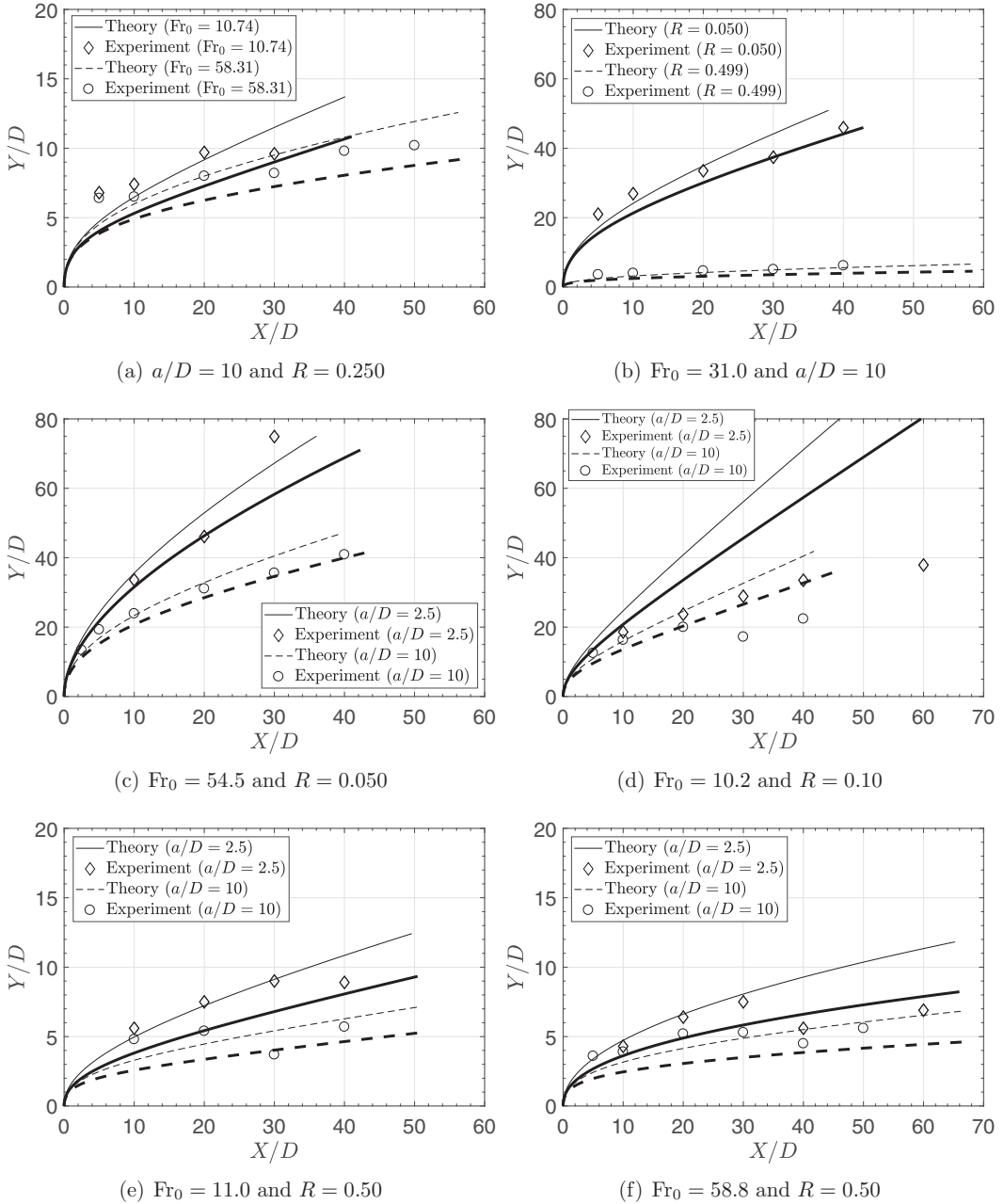
FIG. 16. Effects of varying the source Froude number, $Fr_0$ (a), ambient to plume source velocity ratio, $R$ (b) and port spacing ratio, $a/D$ (c)–(f) on the plume trajectory. The thin curves represent the theory without a drag term (Secs. IV A and IV B) whereas the counterpart thick curves represent the theory of Sec. IV D with $C_D = 1$. The experimental data are taken from Appendix A of Kannberg and Davis [24]. Note that the uppermost diamond in (c) was measured using a different method compared to the other experimental data [24].

worst-case scenarios are to be estimated using the irrotational flow theory described in Secs. II and III. The best-case scenario, corresponding to the merger of two adjacent plumes, is modeled using the geometrical merging criterion proposed by Wu and Koh [19] (cf. Fig. 2 of Ref. [29]).

TABLE I. Representative operating and environmental conditions for the back-to-back and single-row cooling towers illustrated in Fig. 17 [30].

| Variables | Name | Value (unit) |
|---|---|---|
| $P_a$ | Ambient pressure at the top of the cooling tower | 101 325 (Pa) |
| $t_a$ | Ambient temperature | 10 (°C) |
| $RH_a$ | Ambient relative humidity | 80 (%) |
| $t_w$ | Wet cooling temperature | 30 (°C) |
| $t_d$ | Dry cooling temperature | 25 (°C) |
| $w_0$ | Stack exit velocity | 6 (m/s) |
| $D_0$ | Stack exit diameter | 8 (m) |
| $a$ | Horizontal distance in the $x$-axis between cell centers | 15 (m) |
| $b$ | Half of the horizontal distance between cell centers in the $y$-axis | 7 (m) |
| $\frac{\dot{m}_d}{\dot{m}_w}$ | Ratio of the dry to wet air mass flow rate | 0.2 and 0.4 |
| $n$ | Number of cooling tower cells in a single row | 15 |

We follow the governing equations for moist plumes presented in Ref. [29] (see Appendix D) and focus particular attention on the relative humidity (RH) of the plumes discharged from a line of cooling tower cells at the center and at the end points. Figures 18(a) and 18(c) show that, as expected and as concerns fog formation, the visible plume length at the center is greater than that at the end points. This difference is more pronounced for two rows of plumes whereby entrainment is more heavily curtailed. In the case of no fog formation, Figs. 18(c) and 18(d) show that a maximum RH is achieved at a higher elevation for the plume at the center than for the plumes at the end points. This latter case indicates that less entrainment does not necessarily lead to fog formation, but rather slows down the rate of decrease of RH. Note that the model calculation leading to Fig. 18 presumes that the dry and wet air are completely mixed, thus resulting in a radially uniform plume at the source. If complete mixing is not achieved, but neither is a coaxial wet/dry plume structure [31,32], the visible plume length can be greatly enhanced; see Fig. 18(c). Therefore, relatively stringent mixing criteria must be assured within the plenum chamber of back-to-back cooling towers.

## VI. CONCLUSIONS

The present paper has extended a previous formulation of Rooney [4] to model two parallel rows of plumes in a quiescent environment and a single row of plumes in a crosswind. We first note that for all symmetric plume configurations considered so far, the entrainment flux is found to be equal to the strength of the line sink, i.e., $E = m$. For two parallel rows of plumes, we consider both configurations with and without offset. Similar profiles of vertical velocity and volume flux are predicted for those two configurations. In contrast to a single row of plumes, the vertical velocity of plumes in two rows levels off before approaching the far-field limit under a relatively large spacing
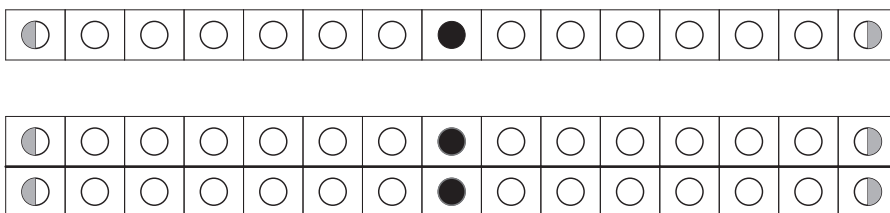


FIG. 17. Top view of single and dual rows of cooling tower cells. The black circles denote cells at the center, and the gray half-circles denote the half-cells at the two ends.
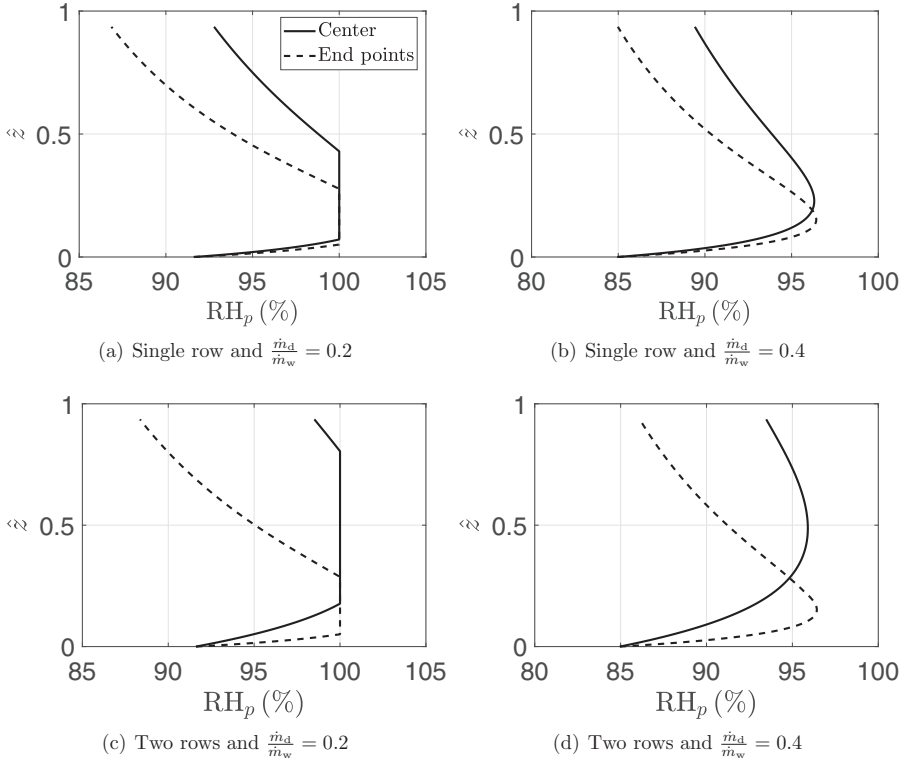
FIG. 18. Relative humidity profiles for single (a),(b) and dual (c),(d) rows of plumes. The model input parameters are specified in Table I. Note, in particular, that $\frac{\dot{m}_d}{\dot{m}_w}$ represents the ratio of dry to wet air mass flow rate.

ratio; see Figs. 6(a) and 6(c). Two different contact heights are defined, and these heights are found to increase approximately linearly with the spacing ratio; see Figs. 8 and 12. For both single and dual rows of plumes, it is found that an effective entrainment perimeter, proportional to the $f$ parameter specified, e.g., in (19), accounts for the reduced entrainment due to plume merger.

Another major contribution of this study is the integral modeling of an infinite row of plumes in a crosswind. In particular, the velocity potential contours remain identical to those in Ref. [4], whereas the modified entrainment closure includes both longitudinal and transverse entrainment. For both modest and strong crosswinds, the theoretical solutions approach the corresponding near- and far-field similarity limits; see Figs. 14(a), 14(b) and 14(d). A comparison of the present theory to the experimental data collected by Kannberg and Davis [24] *vis-à-vis* the plume centerline trajectory yields satisfactory agreement, particularly when the theory is modified as in Sec. IV D to include a drag term; see Fig. 16. It is also noted that a constant drag coefficient model is not able to describe the extreme case of small ambient Reynolds number and port spacing ratio.

The theory of single and dual rows of plumes in a quiescent environment has been applied to cooling tower plumes arising from long rows containing multiple cooling tower cells. The aforementioned theory only applies to plumes discharged from cells at the center, where a minimum of ambient entrainment is expected. A comparison of the relative humidity profiles for plumes at the center versus plumes at the end points is made in Fig. 18. Results drawing from this comparison indicate that a back-to-back configuration may greatly enhance the visible plume length.

Given the rather complicated nature of plume-plume interactions, the coupling presented here between the irrotational flow theory and the integral plume equations may be improved. Key to this

coupling is an entrainment closure that incorporates the nonuniform distribution of the entrainment flow speed along the velocity potential contours. Accounting for such an effect also requires a presumed nonuniform vertical velocity profile that deviates from the "top-hat" profiles considered in the present model.

## ACKNOWLEDGMENTS

## APPENDIX A: ENTRAINMENT FLUX CALCULATION USING THE STREAM FUNCTION

For two-dimensional and incompressible flows, the flux of fluid between two streamlines equals the difference in the stream function. For a single row of line sinks, the stream function is given as

$$\psi = \text{Im}(\Omega) = -\frac{m}{2\pi} \tan^{-1} \left( \frac{\cos x' \sinh y'}{\sin x' \cosh y'} \right). \tag{A1}$$

Using the physical interpretation of the stream function, the rate of entrainment across any contour in Fig. 1 is

$$E = \psi_{(x'_+, y')} - \psi_{(x'_-, y')}. \tag{A2}$$

For $p \leqslant 1$, $y'(x'_+) = y'(x'_-) = 0$, thus $E = -\frac{m}{2\pi}(0 - \pi) = m/2$. For $p > 1$, $\cos x'_\pm = 0$ so that $E = -\frac{m}{2\pi}(0 - \pi) = m/2$.

For the case of dual rows of nonoffset line sinks, the stream function is given as

$$\psi = -\frac{m}{2\pi} \tan^{-1} \left( \frac{\sin 2x' \sinh 2y'}{\cosh 2b' - \cos 2x' \cosh 2y'} \right). \tag{A3}$$

For $p \leqslant \cosh 2b' - 1$, the rate of entrainment across any closed contour is

$$E = 2\big(\psi_{(0, y'_{\max})} - \psi_{(0, y'_{\min})}\big) = -\frac{m}{\pi}(0 - \pi) = m, \tag{A4}$$

where $y'_{\max}$ and $y'_{\min}$ are given by (33) and (34), respectively. For $\cosh 2b' - 1 < p \leqslant \cosh 2b' + 1$,

$$E = 2\big(\psi_{(0, y'_{\max})} - \psi_{(x'_-, 0)}\big) = -\frac{m}{\pi}(0 - \pi) = m. \tag{A5}$$

For $p > \cosh 2b' + 1$,

$$E = 2(\psi_{(0, y'_{\max})} - \psi_{(-\pi/2, y')}) = -\frac{m}{\pi}(0 - \pi) = m. \tag{A6}$$

For the case of dual rows of line sinks with an offset $a/2$, the stream function is given as

$$\psi = -\frac{m}{2\pi} \tan^{-1} \left( \frac{\cos 2x' \sinh 2y' - \sinh 2b'}{\sin 2x' \cosh 2y'} \right). \tag{A7}$$

For $p \leqslant \cosh 2b'$,

$$E = 2\big(\psi_{(0, y'_{\max})} - \psi_{(0, y'_{\min})}\big) = -\frac{m}{\pi}(-\pi/2 - \pi/2) = m, \tag{A8}$$

where $y'_{\max}$ and $y'_{\min}$ are given by (58) and (59), respectively. For $p > \cosh 2b'$,

$$E = (\psi_{(\pi/4, y'_+)} - \psi_{(-\pi/4, y'_+)}) + (\psi_{(-\pi/4, y'_-)} - \psi_{(\pi/4, y'_-)}) = -\frac{m}{2\pi}(-\pi) - \frac{m}{2\pi}(-\pi) = m. \tag{A9}$$

On the basis of the above results, we conclude that $E = m/2$ and $E = m$ for the single and dual rows of plumes, respectively.

## APPENDIX B: COMPARISON BETWEEN THE PRESENT THEORY AND REF. [19]

In a strong crosswind, the plume-plume interactions become less intense than those in a weak crosswind. For a rosette buoyant jet group with a jet-to-riser diameter ratio of the order of 0.1, Lai *et al.* [10] revealed that the dynamic interactions between buoyant jets were negligible even in a moderate crossflow. Therefore, and in cases of moderate to strong crosswinds, we may treat multiple plumes the same as an isolated plume premerger, which is consistent with the model of Wu and Koh [19] (hereafter WK78). WK78 assumes that the plume cross section is perfectly round premerger, and the rate of entrainment is given as

$$E = 2\pi r(\gamma_1|U_p - U_a \cos\theta| + \gamma_2 U_a \sin\theta), \tag{B1}$$

where $r$ is the mean plume radius. Once merger is initiated, the round plume transitions to a slot plume with a rectangular cross section. Thus, the counterpart entrainment rate postmerger is evaluated from

$$E = 2a(\gamma_1|U_p - U_a \cos\theta| + \gamma_2 U_a \sin\theta). \tag{B2}$$

On this basis, and following the nondimensionalization given by (80), Eqs. (75)–(77) can be nondimensionalized to the identical form as (81)–(83) but with $f$ given instead by

$$f = \begin{cases} \pi^{1/2} \dfrac{\overline{Q}^{1/2}}{\overline{a}\,\overline{U}_p^{1/2}}, & \text{(pre-merger)}, \\ 1, & \text{(post-merger)}. \end{cases} \tag{B3}$$

WK78 assumes that merging occurs on the basis of a geometrical criterion, which requires that $r = a/2$. The equivalent nondimensional relation is given as

$$\overline{r} \equiv \left(\frac{\overline{Q}}{\pi \overline{U}_p}\right)^{1/2} = \overline{a}/2, \tag{B4}$$

where $\overline{r}$ denotes the nondimensional plume radius. At the merger height, the round plume evolves to a two-dimensional plume while the plume cross-sectional area remain unchanged.

Figure 19 shows the comparison between the present irrotational flow theory and the WK78 theory in terms of plume trajectory ($\overline{z}$ versus $\overline{x}$) and vertical velocity ($\overline{z}$ versus $\overline{w}$) for $\overline{a} = 0.2, 1$, and 10. The gap between the heights of first contact for the present theory and WK78 increases as $\overline{a}$ increases. This is consistent with the fact that the effect of plume merger weakens with increasing $\overline{a}$. Overall good agreement is observed *vis-à-vis* the plume trajectory; see Figs. 19(a), 19(c) and 19(e). It is intuitive that the present theory should predict greater plume rise than does WK78 because the former theory admits less entrainment than the latter. The above argument applies for the cases $\overline{a} = 0.1$ and 1. However, and in the case of large $\overline{a}$, e.g., $\overline{a} = 10$, Fig. 19(e) shows greater plume rise for WK78 than for the present theory, at least in the near-field region. Correspondingly, the vertical velocity, $\overline{w}$, predicted by WK78 is larger in the range $0 < \overline{z} \lesssim 5$. This nonintuitive result is due to the large near-source entrainment experienced at large wind speeds, which rapidly expands the plume cross section using the irrotational flow theory. By contrast, and for a single plume (premerger using WK78), the entrainment rate actually decreases near the source as the plume is bent over rapidly by a strong wind [cf. Fig. 5(b) of Ref. [21]]. Reassuringly, the present irrotational flow theory avoids the kinks that characterize the vertical velocity profiles as computed using WK78; see Figs. 19(b), 19(d) and 19(f).
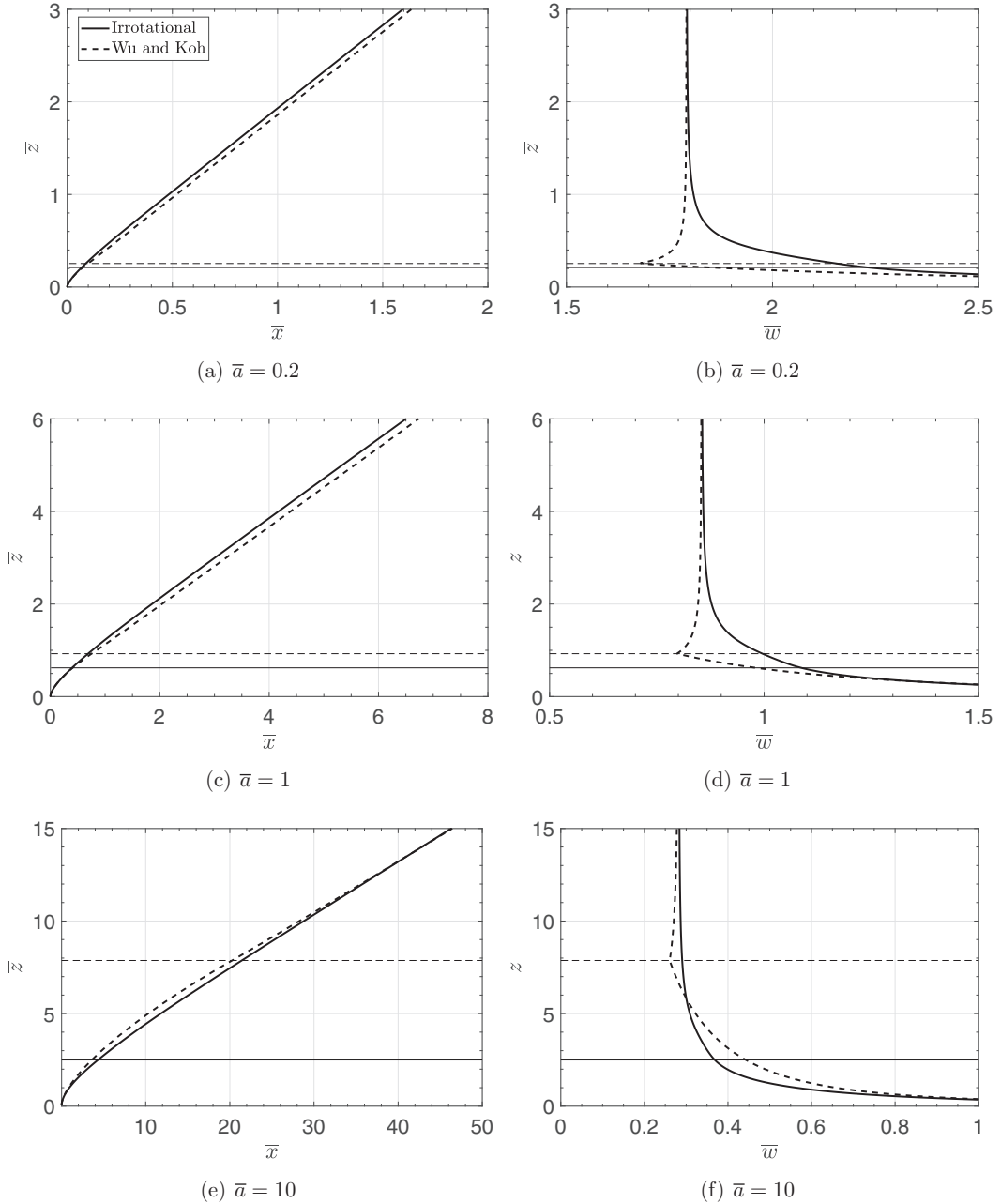
FIG. 19. Comparison between the present irrotational flow theory and the theory of Wu and Koh [19]. The horizontal solid and dashed lines denote the respective heights of first contact for the above theories. In all cases, $\Gamma_0 = 1$.

## APPENDIX C: THEORY VERSUS EXPERIMENT OF A SINGLE PLUME IN A NEUTRAL CROSSWIND

This Appendix attempts to clarify two things: One is whether a constant entrainment coefficient model can successfully predict the trajectory of a single plume in a crosswind; second is a compar-

TABLE II. Experimental conditions for turbulent plumes in neutral crossflows [34]. $D_0$ is the nozzle diameter; $\frac{\rho_0 - \rho_a}{\rho_a}$ is the relative difference between the plume source density ($\rho_0$) and the ambient fluid density ($\rho_a$); $Q_0$ is the plume source volume flux; $U_a$ is the ambient flow speed; $w_0$ is the plume source vertical velocity; and $Fr = w_0/(g_0' D_0)^{1/2}$ is the densimetric Froude number, where $g_0' = g\frac{\rho_0 - \rho_a}{\rho_a}$ is the source reduced gravity.

| Experiment | $D_0$ (mm) | $\frac{\rho_0-\rho_a}{\rho_a}$ | $Q_0$ (L min$^{-1}$) | $U_a$ (cm s$^{-1}$) | $U_a/w_0$ | Fr |
|---|---|---|---|---|---|---|
| 1 | 7 | 0.097 | 0.56 | 4.68 | 0.19 | 2.97 |
| 2 | | | | 8.86 | 0.37 | 2.97 |
| 3 | | | | 13.05 | 0.54 | 2.97 |
| 4 | | | | 21.4 | 0.88 | 2.97 |
| 5 | 7 | 0.097 | 1.00 | 4.68 | 0.11 | 5.31 |
| 6 | | | | 8.86 | 0.20 | 5.31 |
| 7 | | | | 13.05 | 0.30 | 5.31 |
| 8 | | | | 21.4 | 0.49 | 5.31 |
| 9 | 7 | 0.097 | 1.83 | 4.68 | 0.06 | 9.71 |
| 10 | | | | 8.86 | 0.11 | 9.71 |
| 11 | | | | 13.05 | 0.16 | 9.71 |
| 12 | | | | 21.4 | 0.27 | 9.71 |

ison of a circular versus elliptical cross section in terms of predicting plume trajectories. We follow the governing equations, (69)–(74), with the closure condition (78) where $\gamma_1 = 0.1$ and $\gamma_2 = 0.6$. The plume cross-sectional area and the rate of entrainment, assuming a circular or elliptical cross section, are given by

$$A = \pi b^2, \quad E = 2\pi b q_e \quad \text{(circular)}, \tag{C1}$$

$$A = \pi \lambda b^2, \quad E = 2\pi b \left(\frac{\lambda^2 + 1}{2}\right)^{1/2} q_e \quad \text{(elliptical)}, \tag{C2}$$

where in (C1) $b$ is the plume radius and in (C2) $b$ is the minor radius, and $\lambda$ is the ratio of the major to the minor radius. According to the experimental observations of Contini *et al.* [33], $\lambda = 1.2$ is chosen. For the experimental conditions listed in Table II, comparisons of theory versus experiment *vis-à-vis* the mean plume centerline trajectories are illustrated in Figs. 20 and 21. The solid and dashed curves, representing the theoretical solutions assuming circular and elliptical cross sections, respectively, almost coincide with each other. This implies that circular and elliptical cross-section models are equally capable of predicting plume trajectories. In all panels of Figs. 20 and 21, overall satisfactory agreement between theory and experiment is observed, which demonstrates the ability of a constant entrainment coefficient model in describing the bulk dynamics for a plume in crosswind; see also the comparison made in Ref. [20].

## APPENDIX D: MOIST PLUME EQUATIONS

We follow the moist plume equations described in Ref. [29], which read as follows:

$$\frac{dQ}{dz} = E, \tag{D1}$$

$$\frac{dM}{dz} = Ag', \tag{D2}$$

$$\frac{d}{dz}\left(\Theta - \frac{L_v}{c_{pa}}W\right) = 0, \tag{D3}$$

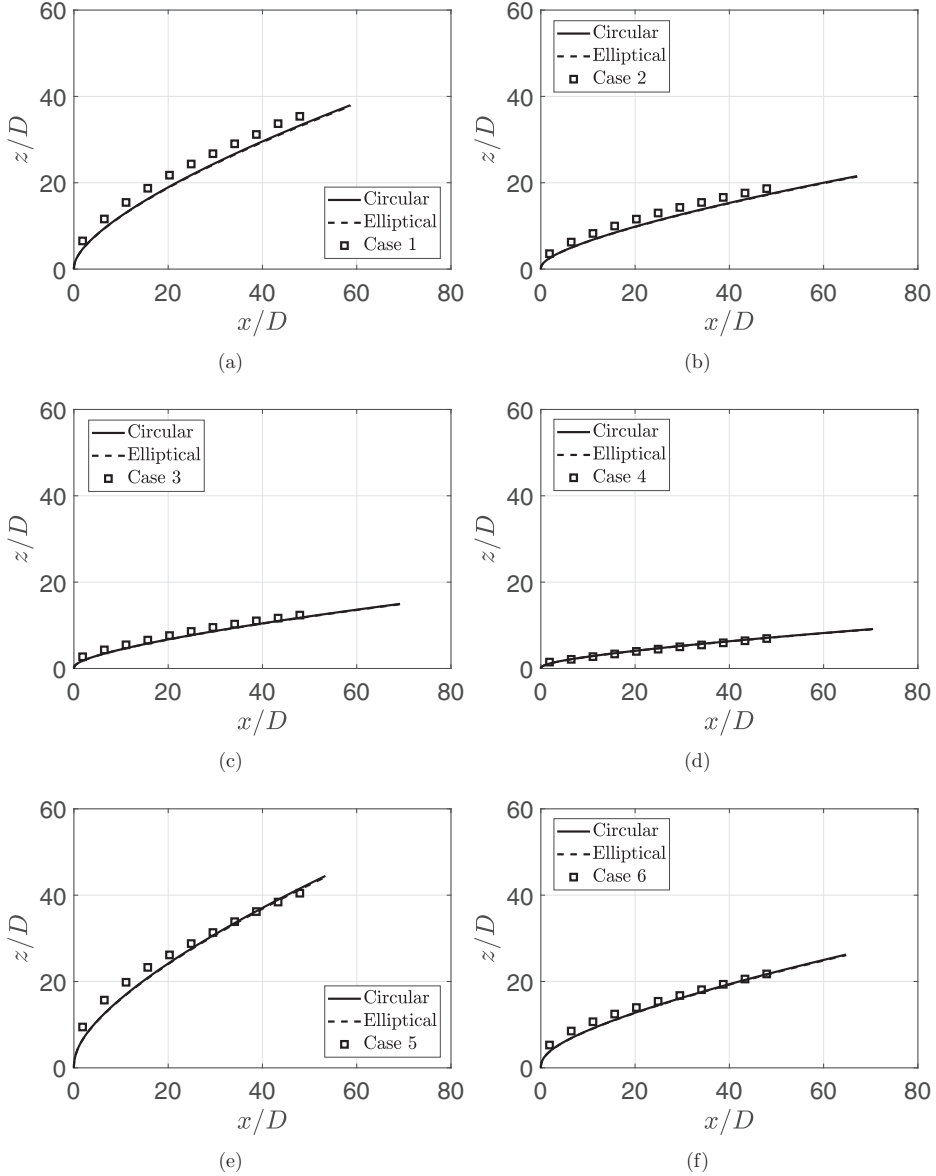$$\frac{d}{dz}(H + W) = 0, \tag{D4}$$

FIG. 20. Comparison between theory and experiment for cases 1–6 of Ref. [34]. The solid and dashed curves nearly overlap except for large $x/D$.

where the volume and momentum fluxes are defined, respectively, as $Q = Aw$ and $M = Aw^2$; the excess temperature flux is $\Theta = Aw(t_p - t_a)$, where $t$ denotes the air dry-bulb temperature; the excess specific humidity flux is $H = Aw(q_p - q_a)$, where $q$ denotes the specific humidity; and the excess specific liquid moisture flux is $W = Aw(\sigma_p - \sigma_a)$, where $\sigma$ denotes the specific liquid moisture. The latent heat of condensation, measured in J/g, is $L_v = L_v(t) = 4.1868\,[597.31 - 0.57\,t]$ with $t$ measured in degrees Celsius, and $c_{pa} = 1.006$ J/(g K) is the specific heat of air at constant pressure [19]. Subscripts $p$ and $a$ denote the plume and the ambient, respectively. The reduced gravity, $g'$, is
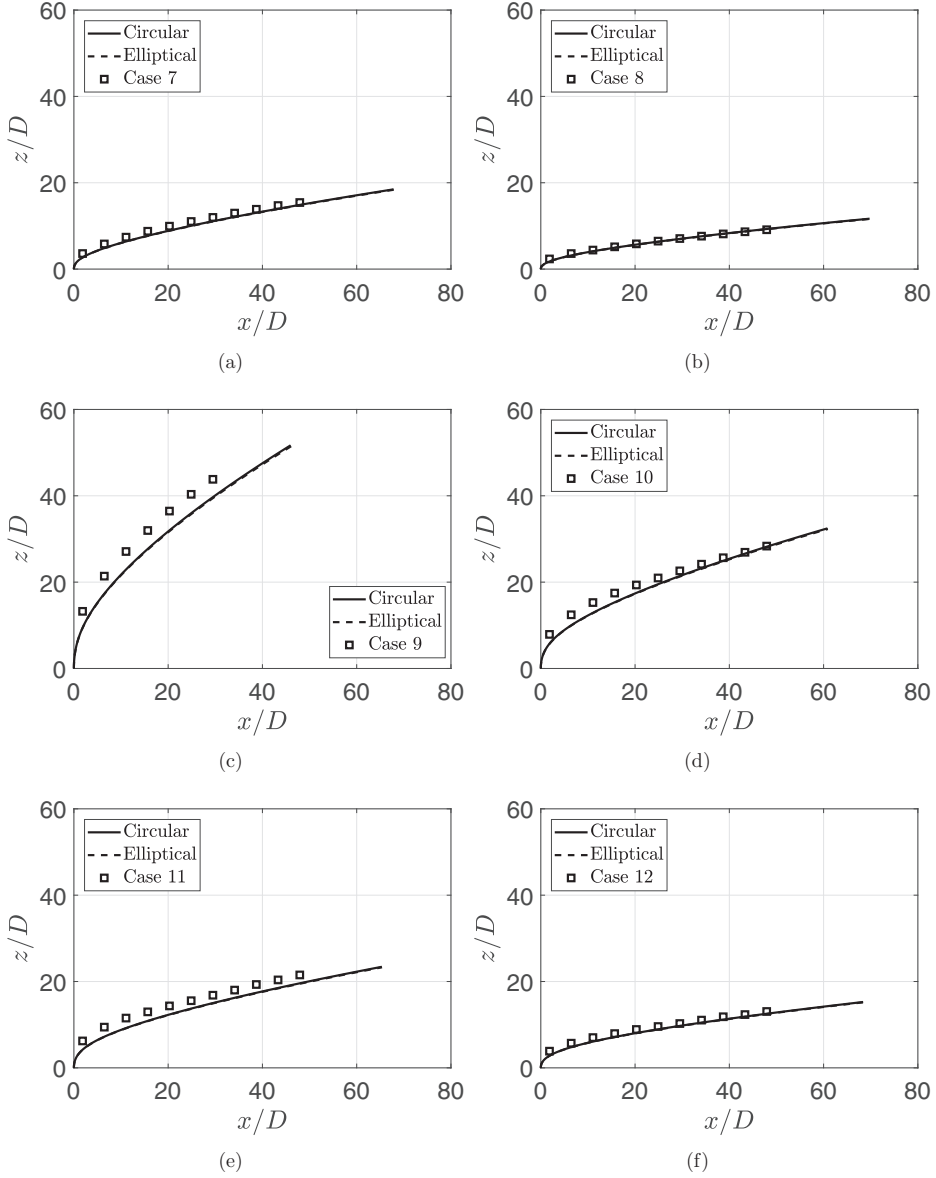
FIG. 21. As in Fig. 20 but for cases 7–12.

defined as

$$g' = g\frac{\rho_a - \rho}{\rho_0} = g\frac{\rho_a - \rho}{\rho_a} = g\left(1 - \frac{t_{v,a}}{t_{v,p}}\right), \tag{D5}$$

where the plume virtual temperature and ambient virtual temperature, $t_{v,p}$ and $t_{v,a}$, are defined, respectively, as follows [35]:

$$t_{v,p} = \left(t_a + 273.15 + \frac{\Theta}{Q}\right)\left[1 + 0.608\left(q_a + \frac{H}{Q}\right) - \frac{W}{Q}\right], \tag{D6}$$

$$t_{v,a} = (t_a + 273.15)(1 + 0.608\,q_a - \sigma_a). \tag{D7}$$

Here, $\sigma_a = 0$ signifies an ambient devoid of liquid moisture. The density of moist air is evaluated using the ideal-gas law, which reads

$$P = \rho R_a t_v, \tag{D8}$$

where $P$ is the total pressure inside/outside the plume, and $R_a = 287.058\,\text{J/kg K}$ is the gas constant of air.

[1] N. Kaye and P. F. Linden, Coalescing axisymmetric turbulent plumes, J. Fluid Mech. **502**, 41 (2004).

[2] C. Cenedese and P. F. Linden, Entrainment in two coalescing axisymmetric turbulent plumes, J. Fluid Mech. **752**, R2 (2014).

[3] P. C. Yannopoulos and G. C. Noutsopoulos, Interaction of vertical round turbulent buoyant jets—Part I: Entrainment restriction approach, J. Hydraul. Res. **44**, 218 (2006).

[4] G. Rooney, Merging of a row of plumes or jets with an application to plume rise in a channel, J. Fluid Mech. **771**, R1 (2015).

[5] A. C. Lai and J. H. Lee, Dynamic interaction of multiple buoyant jets, J. Fluid Mech. **708**, 539 (2012).

[6] P. C. Yannopoulos and G. C. Noutsopoulos, Interaction of vertical round turbulent buoyant jets—Part II: Superposition method, J. Hydraul. Res. **44**, 233 (2006).

[7] P. C. Yannopoulos, Advanced integral model for groups of interacting round turbulent buoyant jets, Environ. Fluid Mech. **10**, 415 (2010).

[8] P. C. Yannopoulos, Superposition model for multiple plumes and jets predicting end effects, J. Geophys. Res.: Atm. **101**, 15153 (1996).

[9] G. A. Briggs, Plume rise predictions, *Lectures on Air Pollution and Environmental Impact Analyses* (American Meteorological Society, Boston, 1975), pp. 59–111.

[10] A. C. Lai, D. Yu, and J. H. Lee, Mixing of a rosette jet group in a crossflow, J. Hydraul. Eng. **137**, 787 (2011).

[11] A. C. Lai and J. H. Lee, Multiple tandem jet interaction in a crossflow, J. Hydrodynam. **22**, 616 (2010).

[12] P. Lindahl and K. Mortensen, Plume abatement–The next generation, CTI J. **31**, 8 (2010).

[13] B. Morton, G. I. Taylor, and J. S. Turner, Turbulent gravitational convection from maintained and instantaneous sources, Proc. R. Soc. London, Ser. A **234**, 1 (1956).

[14] B. Morton and J. Middleton, Scale diagrams for forced plumes, J. Fluid Mech. **58**, 165 (1973).

[15] Z. He and Y. Lou, Integral model for multiple forced plumes arranged around a circle in a linearly stratified environment, Phys. Rev. Fluids **4**, 123501 (2019).

[16] R. Jordinson, *Flow in a Jet Directed Normal to the Wind* (Ministry of Supply, Aeronautical Research Council, London, 1956).

[17] D. Hoult and J. Weil, Turbulent plume in a laminar cross flow, Atm. Environ. (1967) **6**, 513 (1972).

[18] J. W. Bush and A. W. Woods, Experiments on buoyant plumes in a rotating channel, Geophys. Astrophys. Fluid Dyn. **89**, 1 (1998).

[19] F. H. Wu and R. C. Koh, *Mathematical Model for Multiple Cooling Tower Plumes* (US Environmental Research Laboratory, Office of Research and Development, Corvallis, Oregon, 1978).

[20] A. Tohidi and N. B. Kaye, Highly buoyant bent-over plumes in a boundary layer, Atm. Environ. **131**, 97 (2016).

[21] S. Li and M. Flynn, Coaxial plumes in a windy ambient with applications to cooling towers, J. Wind Eng. Indust. Aerodyn. **196**, 104054 (2020).

[22] B. Devenish, G. Rooney, H. Webster, and D. Thomson, The entrainment rate for buoyant plumes in a crossflow, Boundary-Layer Meteorol. **134**, 411 (2010).

[23] G. A. Briggs, Plume rise and buoyancy effects, Atm. Sci. Power Production **850**, 327 (1984).

[24] L. D. Kannberg and L. Davis, *An Experimental/analytical Investigation of Deep Submerged Multiple Buoyant Jets* (US Environmental Research Laboratory, Office of Research and Development, Corvallis, Oregon, 1976).

[25] J. Kennedy and H. Fordyce, Plume recirculation and interference in mechanical draft cooling towers, Cooling Tower Environment-1974, Symposium at University of Maryland 4–6 March 1974, PPSP CPCTP-22 (WRRC Special Report, Univ. of Maryland, 1974).

[26] M. Schatzmann and A. J. Policastro, An advanced integral model for cooling tower plume dispersion, Atm. Environ. (1967) **18**, 663 (1984).

[27] P. K. Kundu, I. M. Cohen, and D. Dowling, *Fluid Mechanics*, 6th ed. (Academic Press, Boston, 2016) pp. 469–532.

[28] L. Kannberg and L. Davis, An analysis of deep submerged multiple-port buoyant discharges, J. Heat Transf. **99**, 648 (1977).

[29] S. Li and M. Flynn, Merging of two plumes from area sources with applications to cooling towers, Phys. Rev. Fluids **5**, 054502 (2020).

[30] D. G. Kröger, *Air-cooled Heat Exchangers and Cooling Towers* (PennWell Books, Tulsa, Oklahoma, 2004).

[31] J. R. Houx, Jr., R. D. Landon, and P. A. Lindahl Jr., Bottom vented wet-dry water cooling tower (1978), US Patent 4,076,771.

[32] S. Li, A. Moradi, B. Vickers, and M. Flynn, Cooling tower plume abatement using a coaxial plume structure, Int. J. Heat Mass Transf. **120**, 178 (2018).

[33] D. Contini, A. Donateo, D. Cesari, and A. Robins, Comparison of plume rise models against water tank experimental data for neutral and stable crossflows, J. Wind Eng. Indust. Aerodyn. **99**, 539 (2011).

[34] D. Contini and A. Robins, Water tank measurements of buoyant plume rise and structure in neutral crossflows, Atm. Environ. **35**, 6105 (2001).

[35] K. A. Emanuel, *Atmospheric Convection* (Oxford University Press on Demand, New York, 1994).